HAL
open science

Crack kinking in a variational phase-field model of brittle fracture with strongly anisotropic surface energy

Bin Li, Corrado Maurini

To cite this version:

Bin Li, Corrado Maurini. Crack kinking in a variational phase-field model of brittle fracture with strongly anisotropic surface energy. Journal of the Mechanics and Physics of Solids, 2019. hal-01983059

HAL Id: hal-01983059

https://hal.sorbonne-universite.fr/hal-01983059v1

Submitted on 16 Jan 2019

HAL is a multi-disciplinary open access archive for the deposit and dissemination of scientific research documents, whether they are published or not. The documents may come from teaching and research institutions in France or abroad, or from public or private research centers.

L'archive ouverte pluridisciplinaire **HAL**, est destinée au dépôt et à la diffusion de documents scientifiques de niveau recherche, publiés ou non, émanant des établissements d'enseignement et de recherche français ou étrangers, des laboratoires publics ou privés.

Crack kinking in a variational phase-field model of brittle fracture with strongly anisotropic surface energy

Bin Li[a,1], Corrado Maurini[a,*]

[a]*Sorbonne Université, CNRS, Institut Jean Le Rond d'Alembert, UMR 7190, F-75005, Paris, France*

Abstract

In strongly anisotropic materials the orientation-dependent fracture surface energy is a non-convex function of the crack angle. In this context, the classical Griffith model becomes ill-posed and requires a regularization. We revisit the crack kinking problem in materials with strongly anisotropic surface energies by using a variational phase-field model. The model includes in the energy functional a quadratic term on the second gradient of the phase-field. This term has a regularizing effect, energetically penalizing the crack curvature. We provide analytical formulas for the dependence of the surface energy on the crack direction and develop an open-source finite-element solver for the higher-order phase-field problem. Quantitative numerical experiments for the crack kinking problem show that the crack kinking directions observed in our phase-field simulations are in close agreement with the generalized maximum energy release rate criterion. Finally, we revisit a thermal quenching experiment in the case of slabs with strongly anisotropic surface energies. We show that the anisotropy can strongly affect the observed crack patterns, either by stabilizing straight cracks or by inducing zig-zag crack patterns. In the case of zig-zag cracks, we observe that crack kinking is always associated with an unstable propagation of a finite length add-crack in a single time-step.

Keywords: Variational fracture, anisotropic materials, phase-field model, crack kinking, brittle fracture, thermal cracks

1. Introduction

Predicting the crack path is of great interest in fracture mechanics as well as industrial and engineering applications. Original applications include the design of easier-to-open packaging (Hamm et al., 2008; Romero et al., 2013; Roman, 2013) or fracture-based fabrication of micro and nanoscale patterns (Nam et al., 2012; Mitchell et al., 2017). The classical theory to predict the crack propagation direction in a quasi-static setting combines the Griffith's propagation criterion (Griffith, 1921) with additional crack path selection criteria, including the maximum circumferential stress (Erdogan and Sih, 1963), the principle of local symmetry (Gol'Dstein and Salganik, 1974; Cotterell and Rice, 1980), and the maximum energy release rate (Hussain et al., 1974). In materials with *isotropic surface energy* these different criteria predict slightly different results (Sumi, 2014), but

*Corresponding author
Email address: corrado.maurini@upmc.fr (Corrado Maurini)
[1]Current address: Sibley School of Mechanical and Aerospace Engineering, Cornell University, Ithaca, NY 14853

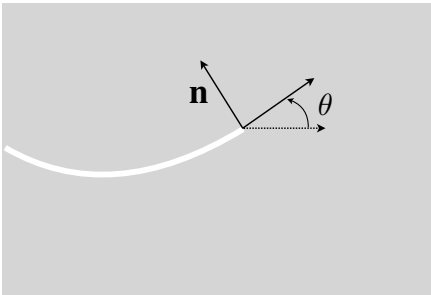

Figure 1: Schematic diagram of the two-dimensional crack advances along angle θ and the unit vector $\boldsymbol{n}$ normal to the crack path.

the relative deviations are almost indistinguishable at the accuracy of the experimental evidences. However, many materials have anisotropic surface energy because of their inherent microstructure or the manufacturing process, which can strongly influence the crack path, such as single crystal (Ball and Payne, 1976; Schultz and Bradt, 1992; Ebrahimi and Hussain, 1995; Azhdari et al., 1998; Ebrahimi and Kalwani, 1999; Marder, 2004), geological materials (Nasseri and Mohanty, 2008; Chandler et al., 2016), engineering materials including rolled aluminium alloy plates (Judt et al., 2015), glass and cellulose fiber reinforced composites (Judt et al., 2018), extruded polymers (Romero et al., 2013; Takei et al., 2013; Ibarra et al., 2016) or apple flesh (Khan and Vincent, 1993). Experimental results clearly show that the crack trajectories in materials with anisotropic surface energy can systematically deviate from the prediction based on the isotropic surface energy assumption (Judt et al., 2015; Ibarra et al., 2016). It is far from obvious how to generalize the different crack direction selection criteria to materials with *anisotropic surface energy* (Marder, 2004; Hakim and Karma, 2005, 2009). If one considers the idealized case of materials with isotropic elasticity and anisotropic surface energy, the principle of local symmetry and stress-based criteria appear to loose their pertinence.

Materials with anisotropic surface energy are characterized by an orientation dependent fracture toughness $G_c(\boldsymbol{n})$, where $\boldsymbol{n}$ denotes the unit vector normal to the crack surface. In the two-dimensional case, the unit normal can be defined by a single angle θ (see Figure 1), and the toughness function can be re-parametrized as $\hat{G}_c(\theta) = G_c(\boldsymbol{n}(\theta))$; in the following, with an abuse of notation, we will omit the hat. Some pioneering works had generalized the maximum energy release rate criterion to anisotropic materials by postulating that cracks propagate along the direction θ^* solution of the following optimization problem (Palaniswamy and Knauss, 1978; Gurtin and Podio-Guidugli, 1998; Marder, 2004):

$$\max_{\theta\in[0,2\pi)} \frac{G(\theta)}{G_c(\theta)}, \tag{1}$$

where $G(\theta)$ is the elastic energy release rate for a crack propagation direction θ. This criterion is denoted as Generalized Maximum Energy Release Rate (GMERR). If the functions $G(\theta)$ and $G_c(\theta)$ are smooth, the first-order optimality condition of (1) reads as $G'(\theta^*) = G_c'(\theta^*)$, where a prime denotes the differentiation with respect to angle θ, and has been identified as a configurational torque balance (Hakim and Karma, 2005, 2009). The critical loading and the crack propagation direction are obtained by combining the crack selection criterion with the critical energy release rate condition $G(\theta^*) = G_c(\theta^*)$. Employing the assumptions of linear elasticity and infinitesimal strain, the

expression of $G(\theta)$ can be calculated using the approximate formula for the stress intensity factors after kinking derived in the seminal work of Amestoy and Leblond (Amestoy and Leblond, 1992). The anisotropy of the surface energy gives rise to crack paths which in general deviate from the direction of maximum energy release rate and deflect towards directions with less energy cost. This general criterion has been verified experimentally very recently in the simple tearing test of brittle polymeric thin sheet with *weakly anisotropic surface energy* (Ibarra et al., 2016), *i.e.* in material where $G_c(\mathbf{n})$ is a convex function of the $\mathbf{n}$. Recent experiments performed by Takei et al. (2013) on tearing of brittle thin sheets with *strongly anisotropic surface energy*, where $G_c(\mathbf{n})$ is a non-convex function, indicate that the observed crack paths can be inconsistent with the global maximization of $G(\theta)/G_c(\theta)$. Reporting crack propagating along metastable directions, the authors suggest a principle based on the local maximization of of $G(\theta)/G_c(\theta)$ on θ rather than global maximization for each $\theta \in [0, 2\pi)$. As pointed out by Gurtin and Podio-Guidugli (1998) and Takei et al. (2013), the GMERR criterion for anisotropic material is analog to the Wulff's graphical construction for the equilibrium shapes of crystal with strongly anisotropic surface energy. The simple energetic models invoking Griffith's theory and GMERR criterion have been remarkably successful in predicting almost quantitatively the crack paths in several tearing experiments on fracture of isotropic (Hamm et al., 2008; Roman, 2013), weakly (Ibarra et al., 2016), and strongly anisotropic brittle thin sheets (Takei et al., 2013). However, its application in a computational framework remains cumbersome and can hardly tackle situation involving the evolution of complex crack patterns. Motivated by the variational nature of simplified models that successfully explain crack paths in tearing sheets, Li et al. (2018) recently presented a variational phase-field model of fracture with isotropic surface energy coupled to a nonlinear thin shell model including stretching and bending which qualitatively and quantitatively reproduced the observed phenomenology. Chambolle et al. (2009) revisited the kinking problem in isotropic and anisotropic materials in the framework of the variational approach to fracture (Francfort and Marigo, 1998). They considered the problem of the quasi-static time-evolution of a pre-existing crack. Their major conclusion is that GMERR is a consequence of a stability criterion on the total energy functional, sum of the elastic and the fracture surface energy. Moreover, they show that crack kinking necessarily implies a jump in time in the evolution: when kinking occurs, the crack necessarily propagates in unstable manner immediately after the kink, with a finite length add-crack in the kinking direction (Chambolle et al., 2009). Their results clearly suggest the variational approach to fracture as an appropriate framework to study fracture in anisotropic media.

In this paper, we study fracture in weakly and strongly anisotropic materials using a phase-field variational model (Bourdin et al., 2008). In two important contributions, Hakim and Karma (2005, 2009) proposed a phase-field model for two-fold weakly anisotropic surface energies and elucidated several features of crack propagation in weakly anisotropic brittle solids. Here, we focus on the crack kinking problem in strongly anisotropic materials, where $G_c(\mathbf{n})$ is non-convex. The problem has many analogies with the theory of moving interfaces in solidification and crystal growth problems with anisotropic surface energy, from which we borrow many results. As pointed out by Gurtin and Podio-Guidugli (1998), the main difference between interface evolution theories and fracture mechanics is that cracks are subjected to an irreversibility condition, that allows previously created cracks to evolve only at the tip. As in solidification theories, sharp interface models with non-convex surface energy becomes ill-posed and require to introduce some form of regularization, for example by penalizing the interface curvature (Herring, 1951; Di Carlo et al., 1992; Gurtin and Jabbour, 2002). An alternative approach, not considered here, is to use relaxed convexified models

(Eggleston et al., 2001). Several phase-field approximations of strongly anisotropic surface energies have been proposed in the context of solidification theories (see Torabi et al., 2009, and references therein). However, not all of them are immediately transposable to phase-field models for fracture, probably because a further main difference between the two theories: while in solidification theories there are two "bulk" phases and an interface, in fracture there is only one "bulk" phase, the other phase, constituting the completely broken material, degenerating into a surface.[2] Here, we adopt and further extend the approach proposed in Li et al. (2015), which is based on higher-order phase-field approximation (Abinandanan and Haider, 2001; Torabi and Lowengrub, 2012). We improve and simplify the phase-field model of Li et al. (2015) while keeping its key properties to allow us for explicit analytical computation of the optimal phase-field localization profile and the dependence of the equivalent surface energy on the crack direction. Hence, we precisely identify and quantify the dependence of the equivalent surface energy on the curvature of the crack. This contribution turns out to be negligible with respect to the energy contribution proportional to the crack length, but has a fundamental regularizing effect in the strongly anisotropic case. We provide[3] an open-source numerical implementation of the proposed phase-field model based on `FEniCS` platform (Alnæs et al., 2015), where the numerical issues associated with the discretization of partial differential equation with higher-order derivatives are solved borrowing special finite element discretization techniques from plate and shell finite element models (Hale et al., 2018). With this infrastructure, we perform numerical experiments to revisit the crack kinking problem in the context of weakly and strongly anisotropic materials. Our results clearly show that the proposed variational phase-field model gives results for the crack propagation direction which are in close agreement with the GMERR criterion, both in the weakly and strongly anisotropic setting. Moreover, they emphasize the presence of forbidden propagation direction and the possible high sensitivity of the propagation direction on the mode-mixity factor and material orientation. To study a controlled crack propagation problem, we revisit in the strongly anisotropic framework the problem of oscillating cracks in quenched plates (Yuse and Sano, 1993, 1997; Yang and Ravi-Chandar, 2001). We identify regimes with the propagation of zig-zig cracks, showing that crack kinking is associated with an unstable propagation including a jump in time and space of the crack evolution, as predicted by Chambolle et al. (2009).

The paper is organized as follows. In Section 2, we briefly recall the variational formulation of the sharp crack model, and then present the models with weakly and strongly anisotropic surface energies. Section 3, after summarizing available variational phase-field models for weakly anisotropic fracture energies, introduces the adopted phase-field model for strongly anisotropic surface energies, discussing its key properties. Section 3.4 succinctly describes the numerical implementation of the model, whilst Section 4 and 5 present and discuss the numerical results for the kinking and quenching problems, respectively. Section 6 collects our final remarks and conclusions.

2. Sharp-interface model of anisotropic brittle fracture

In the variational approach to fracture initiated by Francfort and Marigo (1998), the quasi-static evolution of crack in brittle solids is reformulated in terms of the minimization of a Griffith

[2] Our attempts to use for fracture problem the phase-field model proposed by Torabi et al. (2009) were unsuccessful. We experienced numerical issues, that we attribute to the singularity of the phase-field approximations of the normal in the middle of the localization profile, where the gradient of the phase-field variable vanishes for higher-order phase-field models (for a graphical illustration see the following Figure 4(b)).

[3] `https://bitbucket.org/bin-mech/anisotropic-gradient-damage`

energy functional. Consider a cracked body $\Omega \subseteq \mathcal{R}^n$ with displacement $\boldsymbol{u}$ imposed on a part of its boundary, say $\partial_u \Omega$. The energy functional of the cracked body (Francfort and Marigo, 1998; Ambrosio et al., 2000) reads as

$$\mathcal{E}\left(\boldsymbol{u}, \Gamma\right) = \mathcal{E}_d\left(\boldsymbol{u}, \Gamma\right) + \mathcal{E}_s\left(\Gamma\right) = \int_{\Omega \setminus \Gamma} W(\boldsymbol{u})\, d\Omega + G_0 \int_{\Gamma} \gamma\left(\boldsymbol{n}\right)\, d\mathcal{H}^{n-1}, \tag{2}$$

where $\mathcal{H}^{n-1}$ denotes the $(n-1)$-dimensional Hausdorff measure and Γ is the set of cracks where the displacement fields $\boldsymbol{u} \in H^1\left(\Omega \setminus \Gamma\right)$ can jump. The bulk integral $\mathcal{E}_d\left(\boldsymbol{u}, \Gamma\right)$ in the functional (2) is the elastic energy stored in the cracked solid, $W(\boldsymbol{u})$ being the elastic energy density function. The surface integral $\mathcal{E}_s\left(\Gamma\right)$ represents the anisotropic fracture surface energy in the sense of Griffith's theory of brittle fracture, where $\boldsymbol{n}$ is the field of unit normals to the crack Γ, see Figure 1. Here and henceforth, we decompose the orientation dependent fracture toughness in a scaling factor having the physical dimensions of an energy per unit of surface, G_0, and a dimensionless function of the normal $\gamma(\boldsymbol{n})$, setting $G_c(\boldsymbol{n}) = G_0\, \gamma(\boldsymbol{n})$. The conditions $\gamma(\boldsymbol{n}) = \gamma(-\boldsymbol{n})$ and $0 < c_1 \leq \gamma\left(\boldsymbol{n}\right) \leq c_2$ for any unit normal vector $\boldsymbol{n}$ for some $c_1 \leq c_2$, must be imposed to have a well-defined surface energy. In isotropic materials $\gamma(\boldsymbol{n}) = 1$. In this paper, we consider anisotropic surface energy, but we assume isotropic elasticity. While this assumption is questionable for many real materials, it greatly helps to factor out and understand the key contributions of the anisotropy in the surface term, which is the focus of the present paper. We will consider a linear elastic behaviour before fracture, assuming $W(\boldsymbol{u}) = \mu\, \boldsymbol{\varepsilon}(\boldsymbol{u}) \cdot \boldsymbol{\varepsilon}(\boldsymbol{u}) + \frac{\lambda}{2} \operatorname{tr}(\boldsymbol{\varepsilon}(\boldsymbol{u}))^2$ where $\boldsymbol{\varepsilon}(\boldsymbol{u}) = 1/2\left(\nabla \boldsymbol{u} + \nabla \boldsymbol{u}^{\mathrm{T}}\right)$, λ and μ are Lamé constants, and $\cdot$ denotes the inner product.

2.1. Time-discrete evolution

In the framework of variational approach to fracture, the quasi-static evolution of brittle fracture under the time-dependent loading parametrized by a pseudo-time t, is recast as three principles of irreversibility, global stability and energy balance (Bourdin et al., 2008; Chambolle et al., 2009; Marigo et al., 2016). In consideration of the numerical implementation, we focus on the time-discrete version of the quasi-static crack evolution problem (Francfort and Marigo, 1998). We consider a linearly increasing displacement loading $t\, \bar{\boldsymbol{u}}(x)$ applied on a part of the boundary $\partial_{\boldsymbol{u}} \Omega$ and the discretization $\{0 = t_0 < t_1 < ... < t_N = T\}$ of the time interval $[0, T]$ into $N+1$ time steps. Given the displacement field and the crack set $(\boldsymbol{u}_{i-1}, \Gamma_{i-1})$ at time step t_{i-1}, the solution of time step t_i is sought as the solution of the minimization problem

$$\inf\left\{\mathcal{E}\left(\boldsymbol{u}, \Gamma\right) : \ \boldsymbol{u} \in \mathcal{C}\left(\Gamma, t\right), \ \Gamma_{i-1} \subseteq \Gamma\right\}, \tag{3}$$

where the space of kinematically admissible displacement at time step t is

$$\mathcal{C}\left(\Gamma, t\right) := \left\{\boldsymbol{u} \in H^1\left(\Omega \setminus \Gamma\right), \ \boldsymbol{u}(x) = t\bar{\boldsymbol{u}}(x) \text{ on } \partial_{\boldsymbol{u}} \Omega\right\}, \tag{4}$$

while the admissible crack sets have to satisfy the irreversibility condition $\Gamma_{i-1} \subseteq \Gamma$, precluding crack healing.

The existence of the minimizers for the variational problem (3) is not guaranteed in general (Ambrosio, 1990). In particular, when the surface energy $\gamma\left(\boldsymbol{n}\right)$ is non-convex, energy functional $\mathcal{E}_s\left(\Gamma\right)$ is not lower semi-continuous[4] (Fonseca, 1992). In words, it is possible to construct mini-

[4] A functional I defined on the set $\mathcal{S}$ is lower semi-continuous at $x \in \mathcal{S}$ if and only if for any sequence $x_n \to x$

$$I(x) \leq \liminf_{x_n \to x} I(x_n).$$

mizing sequences of oscillating crack patterns, whose limit has an energy larger that the limit of the energies of the sequence, as it will be explicitly illustrated in the following Remark 2. For this reason, the discussion on the convexity of the surface energy is crucial. We recall below useful criteria to check the convexity of $\gamma(\mathbf{n})$, following Gurtin (1993) and Kobayashi and Giga (2001).

2.2. Convexity of anisotropic surface energy

The dimensionless fracture surface energy function $\gamma(\boldsymbol{n})$ is defined on the unit sphere $\mathcal{S}^{n-1}$, which is not a convex set. To discuss its convexity is technically convenient to consider the one-homogeneous extension of $\gamma(\boldsymbol{n})$ from the unit sphere $\mathcal{S}^{n-1}$ to the whole space $\mathcal{R}^n$ by setting

$$\hat{\gamma}(\boldsymbol{x}) = \begin{cases} \|\boldsymbol{x}\|\,\gamma\left(\frac{\boldsymbol{x}}{\|\boldsymbol{x}\|}\right) = \|\boldsymbol{x}\|\,\gamma(\boldsymbol{n}), & \boldsymbol{x} \neq \mathbf{0} \\ 0 & \boldsymbol{x} = \mathbf{0} \end{cases}, \tag{5}$$

where $\|\boldsymbol{x}\| = \sqrt{\sum_{i=1}^{n} x_i^2}$ is the Euclidean norm, see Figure 2(a). The one-homogeneous function $\hat{\gamma}$ is convex if and only if its level-set $\hat{\gamma}(\boldsymbol{x}) = 1$ is convex, see Rockafellar (1997); Kobayashi and Giga (2001). The level-set $\hat{\gamma}(\boldsymbol{x}) = 1$ is the set of points of $\mathcal{R}^n$ such that $\|\boldsymbol{x}\| = 1/\gamma(\boldsymbol{x}/\|\boldsymbol{x}\|)$, which is called the *Frank plot* of γ:

$$\mathrm{Frank}(\gamma) = \left\{ \frac{1}{\gamma(\boldsymbol{n})}\boldsymbol{n};\ \boldsymbol{n} \in \mathcal{S}^{n-1} \right\} = \{\boldsymbol{x} \in \mathcal{R}^n;\ \hat{\gamma}(\boldsymbol{x}) = 1\}. \tag{6}$$

Throughout this paper, we restrict ourselves to continuous fracture surface energy functions $\gamma(\boldsymbol{n})$, for which the Frank plot defines a closed set, the *Frank diagram* of γ. The interested reader can find further details on the mathematical analysis of anisotropic surface energies in the introductory review paper of Kobayashi and Giga (2001) and in (Gurtin, 1993, 2008).

In the two-dimensional setting, it is more convenient to use polar coordinates and the function $\gamma(\theta)$ can be parametrized with a single angle θ. In polar coordinates, the Frank diagram is the polar plot of $1/\gamma(\theta)$. Its curvature is written as $(\gamma(\theta) + \gamma''(\theta))/\sqrt{(1 + (\gamma'(\theta)/\gamma(\theta))^2)^3}$. The function $\gamma(\theta)$ will lose the convexity whenever the local convexity condition

$$\gamma(\theta) + \gamma''(\theta) \geq 0 \tag{7}$$

is violated for some angle ranges. The quantity $\gamma(\theta) + \gamma''(\theta)$ is referred to as surface stiffness in crystallography literature, which is directly related to the thermodynamic stability of crystal surface (Müller and Métois, 2008). Sekerka (2005) discusses the more complex case of the three-dimensional setting.

The surface energy is called *weakly anisotropic* if the function $\gamma(\boldsymbol{n})$ is *convex* or *strongly anisotropic* if $\gamma(\boldsymbol{n})$ is *non-convex*. The convexity can be assessed graphically by looking for the convexity of the Frank diagram of γ. Figure 2 gives examples of strongly (b) and weakly (c) anisotropic surface energies.

Remark 1. The minimization problem of the Griffith functional is well-posed only for the weakly anisotropic surface energy. For the strongly anisotropic surface energy, one possible strategy to remove the ill-posedness is to regularize the Griffith functional by allowing the fracture surface energy to depend on the mean curvature K of the crack set such that the anisotropic surface energy takes the form

$$\mathcal{E}(\boldsymbol{u}, \Gamma) = \mathcal{E}_d(\boldsymbol{u}, \Gamma) + \mathcal{E}_s(\Gamma) = \int_{\Omega\setminus\Gamma} W(\boldsymbol{u})\, d\Omega + G_0 \int_{\Gamma} \left(\gamma(\boldsymbol{n}) + \frac{\varepsilon^2}{2} K^2 \right) d\mathcal{H}^{n-1}. \tag{8}$$

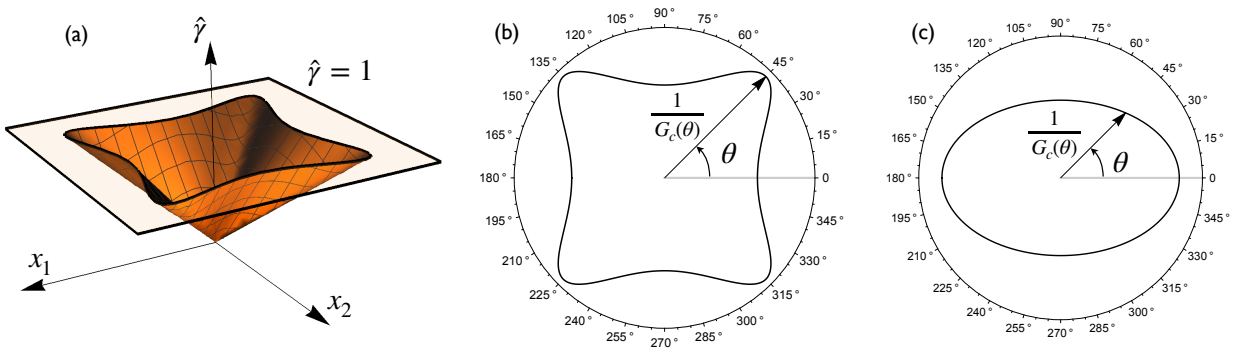

Figure 2: Frank diagram and convexity of the surface energy: (a) Plot of the one-homogeneous extension $\hat{\gamma}$ defined in (5) for the non-convex surface energy $\gamma(\theta) = \sqrt[4]{1 + 0.7\cos 4\theta}$. (b) The corresponding Frank diagram (6) of the anisotropic fracture surface energy enclosed by the level-set $\hat{\gamma} = 1$. (c) The Frank diagram for the convex surface energy $\gamma(\theta) = \sqrt{1 - 0.4\cos 2\theta}$.

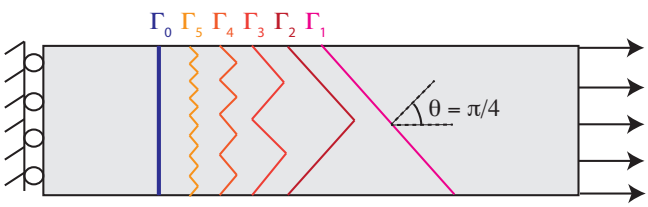

Figure 3: Example of zig-zig crack patterns in the traction problem for a strongly anisotropic bar with a surface energy $G_c(\boldsymbol{n})$ as in Figure 2(a-b). Because of the absence of an intrinsic length-scale, this type of patterns can be used to show the lack of lower semicontinuity of the energy functional $\mathcal{E}_s(\Gamma)$, and hence the lack of existence of solutions to the Griffith problem (3), see Remark 2.

Such a curvature dependence introducing an additional physical length scale ε on which sharp corners are rounded. This explicit form of anisotropic surface energy $\mathcal{E}_s(\Gamma)$ has been introduced for studying the evolution of non-convex interfacial energy (Di Carlo et al., 1992; Gurtin and Jabbour, 2002), which penalizes the high spatial oscillations as well as prevents the surface from forming sharp corners.

Remark 2. In the case of non-convex surface energy, one can easily construct examples showing the lack of lower-semicontinuity of the energy. Consider the case of Figure 2, where $\gamma(\theta) = \sqrt[4]{1 + 0.7\cos 4\theta}$, and the traction problem for a two-dimensional bar of length L and width W, with a material orientation such that $\theta = 0$ corresponds to the axial direction. The maximum and minimum of $\gamma(\theta)$ are $\gamma(0) = \sqrt[4]{1.7}$ and $\gamma(\pi/4) = \sqrt[4]{0.3}$. Referring to Figure 3, the total energy of the solutions with the transversal crack pattern Γ_0 is $G_0\sqrt[4]{1.7}\,W$, whilst the energy of any of the crack patterns $\Gamma_{n>0}$ is $G_0\sqrt[4]{0.3}\,\left(\sqrt{2}W\right)$. The energy is not lower semi-continuous because for $n \to \infty$, the energy of the limit Γ_0 of the Γ_n's, $G_0\sqrt[4]{1.7}W$, is larger than the limit of the energies of the Γ_n's, $G_0\sqrt[4]{0.3}\,\left(\sqrt{2}W\right)$. This means that there are minimizing sequences not converging to a minimizer of the total energy.

3. Phase-field approximations of anisotropic brittle fracture

The direct numerical implementation of Griffith's energy functional (2) is challenging due to the jump discontinuities of $\boldsymbol{u}$ whose locations are unknown *a priori*. To overcome this challenge, Bourdin et al. (2000) resort to a regularization strategy initially developed by Ambrosio and Tortorelli (1990) for solving similar free-discontinuity problems encountered in image segmentation (Mumford and Shah, 1989). In the regularized model, cracks are represented by a scalar phase-field or damage variable, α, which is 1 in a completely broken material point, 0 away from the crack, and varies from 0 to 1 smoothly in a band of finite width representing the smeared representation of the crack. The energy functional of a possibly fractured elastic body with isotropic surface energy is modeled by

$$\mathcal{E}_\ell\left(\boldsymbol{u},\alpha\right) = \int_\Omega a(\alpha)\, W(\boldsymbol{u})\, d\Omega + \frac{G_c}{c_w}\int_\Omega \left(\frac{w(\alpha)}{\ell} + \ell\|\nabla\alpha\|^2\right) d\Omega, \tag{9}$$

where $a(\alpha)$ is a (decreasing) stiffness modulation function and $w(\alpha)$ is an (increasing) function representing the specific energy dissipation per unit of volume. In the following we will assume

$$a(\alpha) = (1-\alpha)^2, \qquad w(\alpha) = \alpha, \tag{10}$$

although different choices are possible, see Pham et al. (2011) and Marigo et al. (2016). The constant G_c is isotropic fracture surface energy, also called the critical energy release rate, whilst $c_w = 4\int_0^1 \sqrt{w(\alpha)}\, d\alpha$ is a normalization constant. This family of functionals is parametrized by a regularization parameter $\ell > 0$ having the physical dimensions of a length and dictating the width of the smeared crack. When ℓ goes to zero, the regularized model converges to the sharp variational theory of brittle fracture in the sense of Gamma-convergence (Bourdin et al., 2000). However, the numerical simulations require a finite value of ℓ, which needs to be resolved by the numerical discretization grid, and are based on *local minimization*, instead of global minimality as in Gamma-Convergence theory. As discussed in Amor et al. (2009); Pham et al. (2011); Tanné et al. (2018), the phase-field model with a fixed internal length and an evolution principle based on meta-stability (local energy minimization) can be regarded as a gradient damage model, where ℓ become a constitutive parameters related to the maximum allowable stress in the material. The success of this phase-field model has prompted a large body of literature in mathematics, continuum mechanics, and computational mechanics that we do not attempt to review here.

3.1. Weakly anisotropic surface energy model

Several generalizations of the phase-field approximation converging to the sharp interface model with weakly anisotropic surface energy have been proposed. Focardi (2001) proved a Gamma-convergence result for a function $\gamma(\boldsymbol{n})$ being a generic norm of the normal $\boldsymbol{n}$, with a minimal modification of the standard Ambrosio-Tortorelli approximation. In short, it consists in replacing the term $\|\nabla\alpha\|$ in (9) with $\gamma(\nabla\alpha)$. This includes the special case where $\gamma(\boldsymbol{n}) = \sqrt{\mathbf{B}\,\boldsymbol{n}\cdot\boldsymbol{n}}$, $\mathbf{B}$ being a symmetric positive-definite second order tensor, for which the phase-field approximation reads as

$$\mathcal{E}_\ell\left(\boldsymbol{u},\alpha\right) = \int_\Omega a(\alpha)\, W(\boldsymbol{u})\, d\Omega + \frac{G_0}{c_w}\int_\Omega \left(\frac{w(\alpha)}{\ell} + \ell\,\mathbf{B}\nabla\alpha\cdot\nabla\alpha\right) d\Omega, \tag{11}$$

and coincides with the weakly anisotropic surface energy studied by Hakim and Karma (2005, 2009). In the following, we will denote by ($\boldsymbol{b}_1$,$\boldsymbol{b}_2$,$\boldsymbol{b}_3$) the orthonormal eigenvectors of $\mathbf{B}$ and by B_i the corresponding eigenvalues. The vectors $\boldsymbol{b}_i$ will constitute the material reference frame.

This anisotropic surface energy model has been extended to fully three-dimensional implementation accounting for geometric nonlinearity and nonlinear elasticity (Clayton and Knap, 2014) and to a multiple phase-field model based on the consideration of several cleavage planes (Nguyen et al., 2017). Recently a different multiple phase-field model accounting for anisotropic degradation has been presented by Bleyer and Alessi (2018) to simulate the non-trivial behavior of cracks in orthotropic materials.

To gain insight into the resulting anisotropic fracture model, let us consider the two-dimensional setting and look for solutions representing a smeared version of a straight crack of orientation θ with respect to the material reference frame, as done in Li et al. (2015). Let us assume that the crack partition the domain Ω in two subdomains with vanishing elastic energy. We set the coordinate frame $(\boldsymbol{x}_0, \boldsymbol{n}, \boldsymbol{t})$, where $\boldsymbol{t} = \cos\theta\, \boldsymbol{b}_1 + \sin\theta\, \boldsymbol{b}_2$, $\boldsymbol{n} = -\sin\theta\, \boldsymbol{b}_1 + \cos\theta\, \boldsymbol{b}_2$ and $\boldsymbol{x}_0$ is an arbitrary point on the crack. We will denote by x and y the coordinates in the normal and tangential directions, such that $\boldsymbol{x} - \boldsymbol{x}_0 = x\, \boldsymbol{n} + y\, \boldsymbol{t}$. To reconstruct the phase-field approximation of a straight crack, we assume that $\alpha = 1$ on $x = 0$ and that α is invariant in the tangential direction, setting $\frac{\partial \alpha}{\partial y} = 0$. Substituting $\nabla\alpha = \|\nabla\alpha\|\, \boldsymbol{n} = \frac{\partial \alpha}{\partial x}\, \boldsymbol{n}$ into (11), the surface energy reduces to

$$\mathcal{E}_s\left(\alpha\right) = \frac{G_c(\theta)}{c_w} \int_\Omega \left(\frac{w(\alpha)}{\ell(\theta)} + \ell(\theta) \left(\frac{\partial \alpha}{\partial x} \right)^2 \right) d\Omega, \tag{12}$$

with

$$G_c(\theta) = G_0 \sqrt{B\left(\theta\right)}, \qquad \ell(\theta) = \ell\, \sqrt{B(\theta)}, \tag{13}$$

being

$$B\left(\theta\right) = \frac{B_1 + B_2}{2} \left(1 - \frac{B_1 - B_2}{B_1 + B_2} \right) \cos 2\theta, \tag{14}$$

Hence, one can reconstruct the optimal damage profile by solving the following bound-constrained minimization problem for α:

$$\inf \left\{ \mathcal{E}_s\left(\alpha\right), \quad 0 \leq \alpha \leq 1 \text{ and } \frac{\partial \alpha}{\partial y} = 0 \text{ on } \Omega, \quad \alpha = 1 \text{ on } x = 0 \right\}. \tag{15}$$

With the choice of $w(\alpha) = \alpha$, following the same procedure as in Pham et al. (2011), one can found that the optimal crack profile in a normal cross-section of the crack is

$$\alpha(x) = \left(1 - \frac{|x - x_0|}{2\ell(\theta)} \right)^2, \quad x \in \left[x_0 - D_0, x_0 + D_0\right], \tag{16}$$

where $D_0 = 2\,\ell(\theta)$ and the diffused crack thickness is $2D_0$, see in Figure 4(a). The resulting equivalent fracture toughness is anisotropic, depending on the orientation θ as in $(13)_1$. In this model, the thickness of the smeared approximation of the crack depends on the orientation. This can pose numerical issues if $B_2 \gg B_1$ (or vice versa). The analytical expression of the thickness in terms of the orientation is useful to set the finite element mesh size relatively to the parameter ℓ and estimate the related discretization errors.

It is easy to verify that the resulting anisotropic surface energy has $G_c\left(\theta\right) + G_c{}''\left(\theta\right) > 0$ in the whole angle range. Hence this model only allows for *weakly anisotropic* surface energy, characterized by an elliptic two-fold Frank plot. The three-dimensional surface energy can be written analogously. This anisotropic surface energy model is too restrictive; for instance, it cannot describe the common

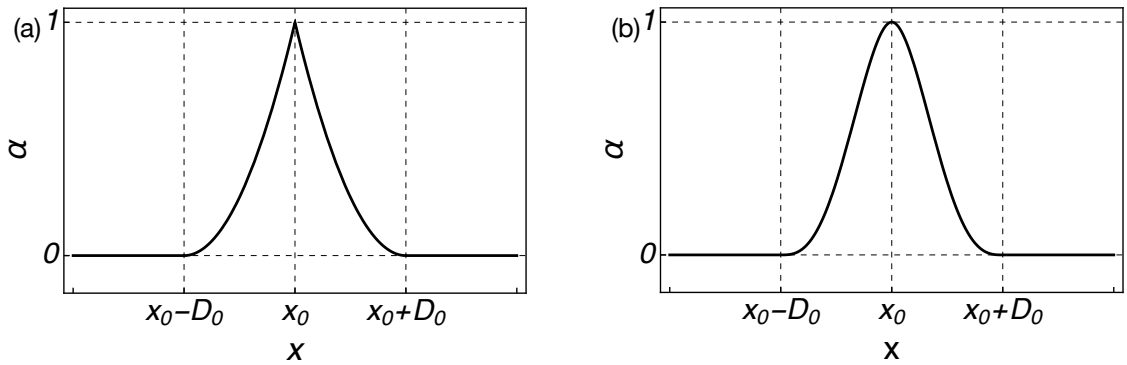

Figure 4: One-dimensional optimal crack profile $\alpha(x)$ centered at x_0 for fully broken elastic bar, the crack thickness is orientation dependent (a) $2D_0 = 4\ell(\theta) = 4\ell\sqrt{B(\theta)}$, (b) $2D_0 = 4\ell(\theta) = 4\ell\sqrt[4]{C(\theta)}$.

cubic symmetry and cannot model strongly anisotropic effects. However, many of the interesting features of fracture in materials with anisotropic surface energy, such as sawtooth crack patterns or forbidden crack directions (Takei et al., 2013), are directly related to the non-convexity of strongly anisotropic surface energies.

3.2. Strongly anisotropic surface energy model

A natural way to produce more general anisotropy is using higher order tensors and derivatives of the phase-field variables. Following this direction, Li et al. (2015) have formulated an anisotropic variational fracture model allowing for both weakly and strongly anisotropic surface energy up to cubic symmetry, which combined the classical variational brittle fracture formulation (9) with the extended Cahn-Hilliard framework proposed in the context of phase-field models of crystal growth (Abinandanan and Haider, 2001). Here, we consider the energy functional

$$\mathcal{E}_\ell(\boldsymbol{u},\alpha) = \int_\Omega a(\alpha)W(\boldsymbol{u})\,d\Omega + \frac{G_0}{c_w}\int_\Omega \left(\frac{w(\alpha)}{\ell} + \ell^3\,\mathbf{C}\,\nabla^2\alpha\cdot\nabla^2\alpha\right)d\Omega, \tag{17}$$

where the $\mathbf{C}$ is a symmetric positive definite fourth order tensor, the $\nabla^2\alpha$ is Hessian matrix expressed as $(\nabla^2\alpha)_{ij} = \frac{\partial^2\alpha}{\partial x_i \partial x_j}$ using index notation, $\cdot$ being here the inner product between second-order tensors.

Differently from the model proposed by Li et al. (2015), the functional used here depends only on the Hessian of the phase-field α, and not on its gradient. Moreover, we assume $w(\alpha) = 9\alpha$ instead of $w(\alpha) = \alpha^2$. The two modifications will allow us to simplify the model and to obtain the analytical solution for the optimal crack profile, keeping the fundamental properties of the phase-field approximation, as it will be shown below. The tensor $\mathbf{C}$ has the same fundamental symmetries as the stiffness tensor in linear elasticity. We consider the orthorhombic case, where the fourth-order tensor $\mathbf{C}$ is characterized by nine independent material constants. In Voigt notation, it reads as

$$\mathbf{C} = \begin{pmatrix} C_{11} & C_{12} & C_{13} & 0 & 0 & 0 \\ C_{12} & C_{22} & C_{23} & 0 & 0 & 0 \\ C_{13} & C_{23} & C_{33} & 0 & 0 & 0 \\ 0 & 0 & 0 & C_{44} & 0 & 0 \\ 0 & 0 & 0 & 0 & C_{55} & 0 \\ 0 & 0 & 0 & 0 & 0 & C_{66} \end{pmatrix}. \tag{18}$$

The necessary and sufficient conditions for the fourth-order tensor $\mathbf{C}$ to be positive definite are (see Mouhat and Coudert, 2014)

$$\begin{aligned} &C_{11} > 0, \quad C_{11}C_{22} > C_{12}^2, \quad C_{44} > 0, \quad C_{55} > 0, \quad C_{66} > 0, \\ &C_{11}C_{22}C_{33} + 2C_{12}C_{13}C_{23} - C_{11}C_{23}^2 - C_{22}C_{13}^2 - C_{33}C_{12}^2 > 0. \end{aligned} \tag{19}$$

Under cubic symmetry, the nine independent constants in (18) further reduce to three by the fact that $C_{11} = C_{22} = C_{33}$, $C_{12} = C_{13} = C_{23}$ and $C_{44} = C_{55} = C_{66}$. The conditions (19) are simplified accordingly.

We derive below the expression for the effective anisotropic surface energy function $G_c(\theta)$ of the phase-field model. To this end, we consider, as in Section 3.1, the two-dimensional setting and solutions in the form of a localization along a straight line in the direction θ with respect to the material axes. Assuming $\frac{\partial \alpha}{\partial y} = 0$ and $\nabla\nabla\alpha = \frac{\partial^2 \alpha}{\partial x^2} \boldsymbol{n} \otimes \boldsymbol{n}$, the surface energy contribution of (17) reduces to

$$\mathcal{E}_\ell^{(s)}(\alpha) = \frac{G_c(\theta)}{c_w} \int_\Omega \left(\frac{w(\alpha)}{\ell(\theta)} + \ell^3(\theta) \left(\frac{\partial^2 \alpha}{\partial x^2} \right)^2 \right) d\Omega, \tag{20}$$

with

$$G_c(\theta) = G_0 \sqrt[4]{C(\theta)}, \qquad \ell(\theta) = \ell \sqrt[4]{C(\theta)}, \tag{21}$$

where for orthorhombic symmetry

$$\begin{aligned} C(\theta) = \frac{3(C_{11}+C_{22}) + 2C_{12} + 4C_{44}}{8} \Bigg(1 + \frac{4(C_{22}-C_{11})}{3(C_{11}+C_{22}) + 2C_{12} + 4C_{44}} \cos 2\theta \\ + \frac{C_{11}+C_{22}-2C_{12}-4C_{44}}{3(C_{11}+C_{22}) + 2C_{12} + 4C_{44}} \cos 4\theta \Bigg), \end{aligned} \tag{22}$$

which is further simplified for cubic symmetry by setting $C_{22} = C_{11}$, giving:

$$C(\theta) = \frac{3C_{11} + C_{12} + 2C_{44}}{4} \left(1 + \frac{C_{11} - C_{12} - 2C_{44}}{3C_{11} + C_{12} + 2C_{44}} \cos 4\theta \right). \tag{23}$$

Solving the one-dimensional problem (20) in the direction $\boldsymbol{n}$ orthogonal to the crack surface (the computations are omitted here) one finds that for $w(\alpha) = 9\alpha$ the damage localized in $[x_0 - D_0, x_0 + D_0]$ and the optimal crack profile reads as

$$\alpha(x) = 1 - \frac{3}{16} \frac{(x-x_0)^4}{\ell^4(\theta)} + \frac{|x-x_0|^3}{\ell^3(\theta)} - \frac{3}{2} \frac{(x-x_0)^2}{\ell^2(\theta)}, \; x \in [x_0 - D_0, x_0 + D_0], \tag{24}$$

where the width of the localization band is finite and given by $D_0 = 2\ell(\theta)$, as illustrated in Figure 4(b). Substituting the optimal crack profile (24) into the energy functional (20), after integration, one find the resulting normalization constant $c_w = 96/5$. The equations above give a full analytical solution for the dependence of the surface energy and the width of phase-field approximation of the crack on the orientation. As a further improvement with respect to the phase-field model proposed in Li et al. (2015), in the present model the phase-field is non-vanishing only in an interval of finite width. By suitably setting the material constant C_{ij}, one can obtain $G_c(\theta) + G_c''(\theta) < 0$ in certain angle ranges. This model can simulate the feature of brittle fracture with strongly anisotropic surface energy, as illustrated in Figure 2(b). This procedure is generalizable to the three-dimensional context, although this is not reported here.

3.3. The intrinsic curvature energy

The anisotropic fracture surface energy term of functional (17) includes a dependency on the Hessian of phase-field. One can expect this term to introduce a dependence of the surface energy on the curvature of the crack. This additional energy contribution can play an important role in penalizing crack kinking and regularizing the fracture model. For this reason, this section is devoted to the analysis of the equivalent fracture surface energy of a curved crack.

To quantify the implicit curvature energy, we consider the isotropic version of the energy functional (17), where the surface energy functional reduces to

$$\mathcal{E}_\ell^{(s)}(\alpha) = \frac{G_0}{c_w} \int_\Omega \left(\frac{w(\alpha)}{\ell} + \ell^3 \left(\nabla^2 \alpha\right)^2 \right) d\Omega, \tag{25}$$

which corresponds to one of the two models studied by Burger et al. (2015). Let us adopt a polar coordinate system (ρ, θ) and consider a circular crack of radius ρ_0. We look for a solution of the phase-field model localized in the annulus $\mathcal{S} = (\rho_0 - D^-, \rho_0 + D^+) \times [0, 2\pi]$ with $w(\alpha) = 9\alpha$, where the thickness parameters D^- and D^+ have to be determined, see the inset of Figure 5. We assume that the phase-field is independent of the polar angle θ and $\alpha(\rho_0, \theta) = 1$. Looking for the minimizers of the energy (25), one finds that the optimal crack profile should be the solution of the following boundary value problem

$$\begin{cases} \dfrac{9\rho}{\ell} + \dfrac{2\ell^3}{\rho^2}\alpha'(\rho) - \dfrac{2\ell^3(\rho)}{\rho}\alpha'' + 4\ell^3\alpha'''(\rho) + 2\ell^3\alpha''''(\rho) = 0 \quad \text{on} \quad \mathcal{S}, \\ \alpha\left(\rho_0 - D^-\right) = \alpha\left(\rho_0\right) - 1 = \alpha\left(\rho_0 + D^+\right) = 0, \\ \alpha'\left(\rho_0 - D^-\right) = \alpha'\left(\rho_0\right) = \alpha'\left(\rho_0 + D^+\right) = 0, \\ \alpha''\left(\rho_0 - D^-\right) = \alpha''\left(\rho_0 + D^+\right) = 0. \end{cases} . \tag{26}$$

Substituting the solution of equations (26) into the surface energy term of the functional (17) expressed in polar coordinates, we obtain the surface energy of the circular crack, say $\mathcal{E}_\ell$. In a Griffith model, this energy should be proportional to the length of the crack, being given by $\mathcal{E}_\mathrm{G} = 2\pi\rho_0 G_0$.

We investigate the implicitly embedded bending energy of the circular crack when varying the dimensionless crack curvature $\kappa = \ell/\rho_0$. We define the relative bending energy as $E_\mathrm{b} = (\mathcal{E}_\ell - \mathcal{E}_\mathrm{G})/\mathcal{E}_\mathrm{G}$. For the present model, this difference is found to be null for a straight crack.

Figure 5 reports the value of E_b as a function of the dimensionless radius of the crack ρ_0/ℓ in log-log scale. An important observation from Figure 5 is that the implicit curvature energy is well characterized by a power law, $E_\mathrm{b} \propto \kappa^\beta$, with a exponent $\beta \approx 2.0$, approaching to zero as $\rho_0/\ell \to \infty$.

These results give the following indications on the equivalent surface energy of the model (25): (i) for straight cracks it is proportional to the crack length, as the classical model (9) penalizing the gradient of α; (ii) for curved cracks, in addition to the dominating term proportional to the crack length, it includes a small contribution proportional to the square of the dimensionless crack curvature, ℓ/ρ_0, see Figure 5. This additional contribution vanishes for $\ell \to 0$. This is consistent with the results of the recent work of Burger et al. (2015), which shows that the isotropic version of energy functional (17) is an elliptic approximation of the Mumford-Shah functional in the sense of Gamma-Convergence, and hence, in the limit $\ell \to 0$, has a surface energy proportional to the crack length and independent of the crack curvature. For the classical model (9) penalizing the

gradient of α, one can easily show that the surface energy is independent of the curvature even for a finite ℓ, since the Euler-Lagrange equations for finding the optimal crack profile results to be identical in both Cartesian and polar coordinates.

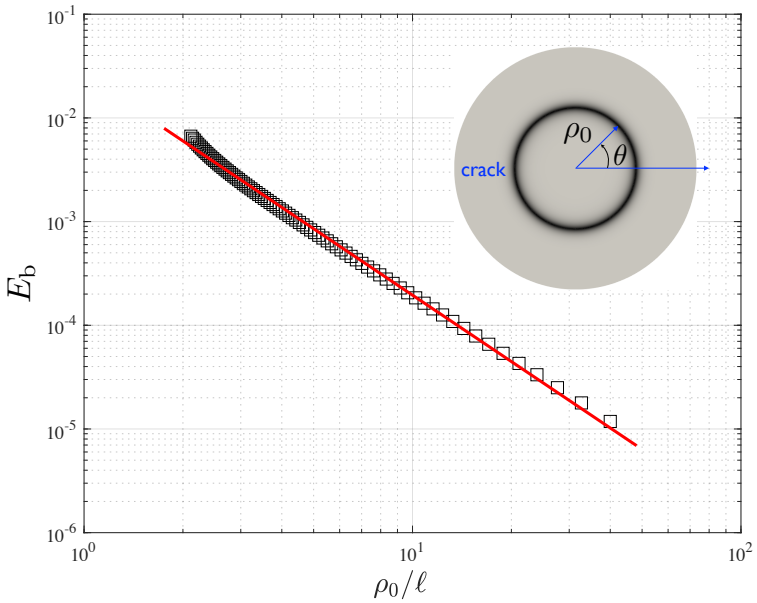

Figure 5: The log-log plot of the relative bending energy $E_b = (\mathcal{E}_\ell - \mathcal{E}_G)/\mathcal{E}_G$ as a function of the radius ρ_0/ℓ of a circular crack. Squares: numerical results from the solution of (26). Red line: Power law $E_b = c\,(\rho_0/\ell)^{-2}$, with $c = 0.026$.

Remark 3. We expect that the Gamma-convergence result of Burger et al. (2015) for the isotropic surface energy (25) can be extended to the weakly anisotropic case, as done by Focardi (2001) for the standard Ambrosio-Tortorelli functional. However, for strongly anisotropic surface energy, the sharp-interface model (2) is not well-posed, because of the lack of semi-continuity. Hence, Gamma-convergence could be eventually expected only to the relaxed convexified version of the strongly anisotropic sharp-interface model (2). The strongly anisotropic phase-field model (17) developed in current work is an intrinsic regularized approximation of Griffith's functional (2). For each fixed crack direction it provides a regularization of the Griffith model with strongly anisotropic surface energy, which can be used to perform numerical simulations also when the crack orientation is left free.

3.4. Numerical implementation

In the following sections, we will perform numerical experiments using the phase-field models with weakly and strongly anisotropic surface energy introduced in Section 3.1 and 3.2. The numerical implementation of the weakly anisotropic model does not present any specific difficulty. The techniques developed for the isotropic case, which are not detailed here, are immediately applicable. We refer the interested reader to previous publications on the isotropic model for further information on the adopted implementation (Bourdin, 2007; Farrell and Maurini, 2017; Tanné et al., 2018) and available open-source codes[5]. We focus instead on the case of models with strongly anisotropic

[5]See `https://bitbucket.org/cmaurini/gradient-damage` by Tianyi Li and Corrado Maurini, `https://bitbucket.org/pefarrell/varfrac-solvers` by Patrick Farrell and Corrado Maurini for `python` implementations

surface energies, which is more complex, and not implemented elsewhere in the present form.

The energy functional of the strongly anisotropy model (17) involves the full Hessian of the phase-field variable, therefore the Galerkin discretization approach necessitates a C^1 continuous approximation scheme. The problem is analogous to the one arising in structural plate and shell models, for which a wealth of techniques have been developed. The previous works on higher-order phase-field models by Borden et al. (2014) and Li et al. (2015) are based on isogeometric analysis with adaptive local refinement (de Borst and Chen, 2018) and smooth mesh-free basis functions, respectively. Alternatives include subdivision surface finite elements (Li et al., 2018) or Mixed Interpolation of Tensorial Components (MITC) formulation (Durán and Liberman, 1992; Chapelle and Bathe, 2010), among others. Here we adopt the MITC method proposed by Durán and Liberman (1992), in the form recently implemented in Hale et al. (2018). We approximate the points of stationarity of the functional (17) by the points of stationarity of the following discretized functional

$$\mathcal{E}_\ell(\boldsymbol{u}_h, \alpha_h, \mathbf{a}_h; \mathbf{s}_h, \mathbf{p}_h) = \int_{\Omega_h} W(\boldsymbol{\varepsilon}(\boldsymbol{u}_h), \alpha_h)\, d\Omega_h + \frac{G_0}{c_w} \int_{\Omega_h} \left(\frac{w(\alpha_h)}{\ell} + \ell^3\, \mathbf{C}\, \nabla \mathbf{a}_h \cdot \nabla \mathbf{a}_h \right) d\Omega_h$$
$$+ \kappa \int_{\Omega_h} \|\mathbf{s}_h\|^2\, d\Omega_h + \int_{\text{edges}} ((\nabla \alpha_h - \mathbf{a}_h - \mathbf{s}_h) \cdot \tau)(\mathbf{p}_h \cdot \tau) dS_h, \quad (27)$$

where $\mathbf{u}_h$ and α_h are the finite element approximations of the displacement and damage field, whilst $(\mathbf{a}_h, \mathbf{s}_h, \mathbf{p}_h)$ are additional vector-valued variables, defined on the finite element mesh Ω_h. We adopt a mesh composed of triangular elements. Following Durán and Liberman (1992); Hale et al. (2018), the displacement $\mathbf{u}$ and the damage α are discretized with standard Lagrange elements of order 1 (P_1), $\mathbf{a}$ is discretized with quadratic Lagrange elements (P_2), whilst $\mathbf{s}_h$ and $\mathbf{p}_h$ are discretized with Nedelec elements of the first-kind[6] of order one (NED_1). The last integral of (27) is taken on the edges of all the elements, where τ denotes the tangent vector to each edge. This term serves to "tie" in a special weak-sense the field $\mathbf{s}_h$ to the difference $\nabla \alpha_h - \mathbf{a}_h$ through the Lagrange multiplier field $\mathbf{p}_h$. For $\kappa \to \infty$, the third integral in (27) imposes $\mathbf{s}_h$ to be almost null. Hence, $\mathbf{a}_h$ and $\nabla \mathbf{a}_h$ turns out to be an approximation of the gradient of the phase-field and its Hessian, respectively. With the specific discretization detailed above, this mixed formulation assures the stability of the discretization scheme and prevents "locking" for large values of the penalty constant κ. We refer the interested reader to Durán and Liberman (1992) for a theoretical proof of the convergence for the case of plates and to Hale et al. (2018) for numerical experiments.

As in the isotropic case, we adopt a staggered approach for the solution of the whole non-linear problem. In the time-discrete evolution, given the damage field $\alpha_h^{(i-1)}$ at the time-step t_{i-1}, the solution at the at each time-step t_i is found by solving the stationarity conditions for the functional (27) under the unilateral constraint $\alpha \geq \alpha_h^{(i-1)}$. We split the whole problem in a "displacement" sub-problem, consisting in the minimization for $\mathbf{u}_h$ once fixed all the other variables, and in a "damage" sub-problem, consisting in the solution for $(\alpha_h, \mathbf{a}_h, \mathbf{s}_h, \mathbf{p}_h)$ at fixed $\mathbf{u}_h$. The two sub-problems are solved iteratively, at each time-step, until a convergence criterion is met.

In two dimensions, the total number of degrees of freedom for each element is 6 for the displacement problem and 21 for the damage problem, including 3 for α, 12 for $\mathbf{a}$, 3 for $\mathbf{s}$, and 3

based on the `FEniCS` (Alnæs et al., 2015) library and `PETSc` (Balay et al., 2016), or `https://bitbucket.org/bourdin/mef90-sieve` by Blaise Bourdin for a `FORTRAN90` implementation based on `PETSc` only.

[6] Nedelec elements of order 1 are finite elements for vector valued fields having as degree-of-freedom the tangential component of the field with respect to the edges of the element.

for $\mathbf{p}$. However, $\mathbf{s}_h$ and $\mathbf{p}_h$ are local variables and can be eliminated through an element-wise local projection technique assimilable to static condensation. Our implementation, based on the `FEniCS` (Alnæs et al., 2015) computing platform, exploits the specific assembling tool developed in `fenics-shells` (Hale et al., 2018), that includes automatic static condensation in the matrix assembling procedure.

Although the functional (27) is at most quadratic in $(\alpha_h, \mathbf{a}_h, \mathbf{s}_h, \mathbf{p}_h)$, the damage sub-problem includes a unilateral constraint on the damage, due to the irreversibility condition $\alpha \geq \alpha_h^{(i-1)}$. Solving the associated variational inequality requires a dedicated non-linear solver. For this task we use the variational inequality solver `SNESVI` distributed in the `PETSC` library (Balay et al., 2016). For further details on this point we refer the reader to Farrell and Maurini (2017), which give specific informations on the use of the `SNESVI` solver in the contest of the variational phase-field models.

The use of the `FEniCS` framework allows us to have a concise and efficient parallel open-source implementation of the finite element model in few hundreds lines of `python` code, which is distributed as supplementary material of the present paper[7]. The code is sufficiently expressive to be used as a further reference for the readers interested in the details of the numerical implementation.

4. Crack kinking with anisotropic surface energy

The variational nature of the phase-field model suggests that the underlying crack path selection principle is related to the GMERR criterion (Chambolle et al., 2009). In the first set of simulations, we verify this hypothesis in the two dimensional setting by comparing the crack propagation kinking direction observed in the simulations with the predictions of the GMERR criterion, varying the mode-mixity factor and material orientation.

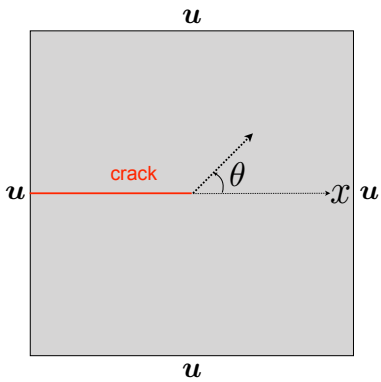

Figure 6: The geometry for the numerical experiments on crack kinking. We apply on the boundary the displacement corresponding to the asymptotic crack field with given mode-I (K_{I}) and mode-II (K_{II}) stress intensity factors. The initial crack is modeled as a very sharp notch.

We consider a squared plate with an initial crack modeled as a geometric feature. We impose on the boundary of the whole domain the displacements corresponding to the singular stress field around the initial straight crack tip parametrized by the stress intensity factors K_{I} and K_{II}. These expressions are recalled in the appendix (A.1), for convenience. For all the simulations performed

[7] `https://bitbucket.org/bin-mech/anisotropic-gradient-damage`

in this Section, we consider non-dimensional parameters, setting the side length of the domain to $L = 1.0$, Young's modulus $E = 1.0$, and scaling fracture toughness $G_0 = 1.0$. The Poisson's ratio is set to $\nu = 0.3$.

4.1. GMERR analytical criterion for the optimal crack propagating direction

In two-dimensional case, the anisotropy of fracture surface energy is characterized by the function $G_c(\theta)$. The GMERR criterion (Palaniswamy and Knauss, 1978; Gurtin and Podio-Guidugli, 1998; Marder, 2004; Hakim and Karma, 2009; Chambolle et al., 2009) postulates that the crack will propagate along the direction θ such that $G(\theta)/G_c(\theta)$ is maximal among all $\theta \in [-\pi, \pi]$. Recalling that during the quasi-static crack propagation the Griffith's criterion

$$G(\theta) = G_c(\theta) \tag{28}$$

must be satisfied, assuming the functions $G(\theta)$ and $G_c(\theta)$ to be smooth, the first-order optimality condition results in

$$\frac{dG(\theta)}{d\theta} = \frac{dG_c(\theta)}{d\theta}. \tag{29}$$

Hakim and Karma (2005, 2009) identified (29) as a configurational torque balance condition. In anisotropic materials the crack paths can deviate from the direction of maximal energy release rate, and deflect towards directions of minimal toughness. The above conditions are a compromise between the maximization of the release rate of the elastic energy and the minimization of the surface energy dissipation. In the isotropic setting, where G_c is independent of direction θ, the right hand side of (29) vanishes and the GMERR reduces to the classical maximum energy release rate criterion. To predict the crack paths based on GMERR, it is essential to calculate $G(\theta)$ and $G'(\theta)$. For linear elastic bulk materials, the energy release rate $G(\theta)$ of a crack kinking out the plane of the parent crack at an angle θ and with a vanishing extension of length is given by the following extension (see e.g. Ichikawa and Tanaka, 1982) of the classical Irwin formula

$$G(\theta) = \frac{\tilde{K}_{\mathrm{I}}^2(\theta)}{E'} + \frac{\tilde{K}_{\mathrm{II}}(\theta)^2}{E'}, \tag{30}$$

where $E' = E$ for plane stress and $E' = E/(1-\nu^2)$ for plane strain. The $\tilde{K}_{\mathrm{I}}$ and $\tilde{K}_{\mathrm{II}}$ are new stress intensity factors (SIFs) at tip of the putative crack with a vanishing extension of length, which can be expanded as a linear combinations of the SIFs K_{I} and K_{II} at the parent crack tip (Amestoy and Leblond, 1992). The full expressions of the new SIFs are provided by (A.2) and (A.3) in the Appendix A. The conditions (28) and (29) are nonlinear algebraic equations, hence their solution can be not unique and can depend on the initial guess. A graphical construction introduced in Gurtin and Podio-Guidugli (1998); Takei et al. (2013); Ibarra et al. (2016) greatly facilitates the prediction of the crack directions. For a given mode-mixity factor $K_{\mathrm{II}}/K_{\mathrm{I}}$, it consists in superposing to the Frank plot of the fracture toughness, *i.e.* the polar plot of $G_c^{-1}(\theta) := 1/G_c(\theta)$, the Frank plot of the energy release rate, *i.e.* the polar plot of $G^{-1}(\theta) := 1/G(\theta)$, see also Section 2.2. For a fixed mode-mixity factor $K_{\mathrm{II}}/K_{\mathrm{I}}$, the smallest value of K_{I} for which the two curves intersect and meet a tangency condition gives the critical loading for the crack propagation and the crack propagation angle. Here we apply this technique to obtain reference solutions for the verification of the results of the phase-field model. Examples of application of this graphical method to the weakly and strongly anisotropic cases are given in the following Figures 7-11, where the black-solid closed curves are the Frank diagram $G_c^{-1}(\theta)$ of the fracture toughness and blue-solid curve is the

Frank diagram $G^{-1}(\theta)$ of the energy release rate. As the load increases, the curve $G^{-1}(\theta)$ comes closer to the origin. The Griffith's criterion (28) is satisfied at any intersection of the curve $G^{-1}(\theta)$ with the ${G_c}^{-1}(\theta)$ curve. The criterion (29) implies that the crack propagation occurs at the first tangent point, defining the critical loading and the direction of crack propagation.

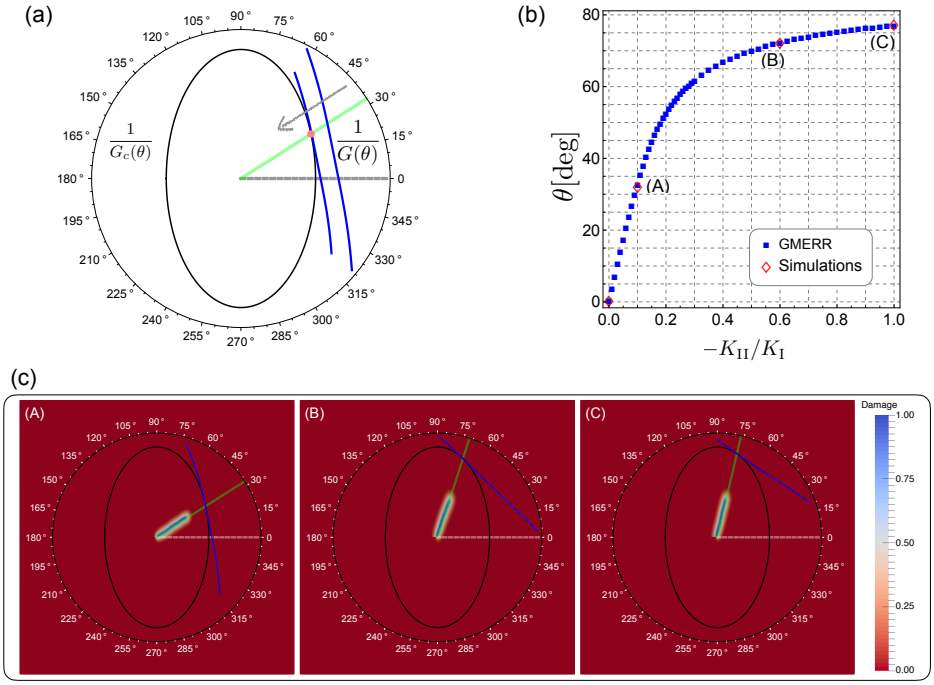

Figure 7: (a) The graphical construction of the GMERR condition (28) and (29) with weakly anisotropic fracture surface energy $G_c(\theta) = \sqrt{1.0 + 0.5\cos 2\theta}$ in polar coordinates. (b) The comparison of the directions of crack propagation observed in phase-field simulations with the predictions of the GMERR criterion. (c) The selected phase-field simulations with different mode-mixity factors: (A) $K_{\rm II}/K_{\rm I} = -0.1$, (B) $K_{\rm II}/K_{\rm I} = -0.6$, (C) $K_{\rm II}/K_{\rm I} = -1.0$, on which the corresponding graphical constructions are superposed.

4.2. Weak anisotropy: effect of the mode-mixity factor $K_{\rm II}/K_{\rm I}$.

We revisit the kinking problem in the case of weakly anisotropic surface energies, studied by Hakim and Karma (2009). Hakim and Karma (2009) compared the simulation results of their phase-field model to the theoretical prediction of the GMERR criterion and a force balance condition. We perform here the simulations with different mode-mixity factors $K_{\rm II}/K_{\rm I}$, using the weakly anisotropic model (11), assuming the principal material direction $\boldsymbol{b}_1$ parallel to the initial crack. We set the parameters $B_{11} = 0.5$ and $B_{22} = 1.5$ in (14) such that the fracture surface energy is $G_c(\theta) = G_0\sqrt{1 + 0.5\cos 2\theta}$. The corresponding Frank diagram is the black ellipse sketched in Figure 7. The length scale parameter ℓ is set to 0.0125. According to $(13)_2$ the maximal and minimal half-width of the smeared approximation of the crack are $D_{\min} = \sqrt{2}\ell$ and $D_{\max} = \sqrt{6}\ell$. We set the mesh size to $\ell/5$. For a fixed mode-mixity factor $K_{\rm II}/K_{\rm I}$, the loading parameter is given by $K_{\rm I}$. Figure 7(b) shows the comparison of the directions of crack propagation observed in phase-field simulations with the predictions of the GMERR criterion. The snapshots of the selected phase-field simulations with different mode-mixity factors: (A) $K_{\rm II}/K_{\rm I} = -0.1$, (B) $K_{\rm II}/K_{\rm I} = -0.6$, (C) $K_{\rm II}/K_{\rm I} = -1.0$. For each case, we superpose the corresponding graphical constructions of the

GMERR conditions (28) and (29). The crack propagation directions predicted by the GMERR criterion are indicated by the green lines in Figure 7. Clearly, the figure 7(b) and (c) show that the directions of crack propagation observed in phase-field simulations match very well with the predictions of the GMERR criterion.

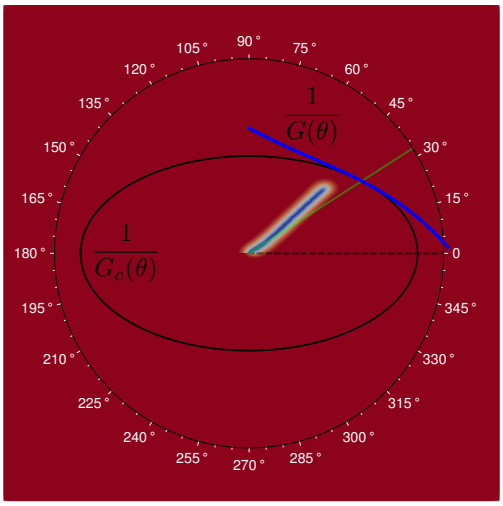

Figure 8: Weakly anisotropic fracture surface energy $G_c(\theta) = \sqrt{1.0 - 0.5\cos 2\theta}$ with $K_{\mathrm{II}}/K_{\mathrm{I}} = -2$. The snapshot for $K_{\mathrm{I}} = 1.5K_{\mathrm{Ic}}$ shows that the crack path will bend during the propagation. We define the crack propagation direction at the initiation as the tangent to the path close to the initial crack tip.

We focus on the initial crack direction immediately after the initiation and not on the full crack path. For this reason, we define the crack direction predicted by the phase-field model as the tangential direction emerging from the initial crack tip immediately after crack initiation. If the simulation is run for larger loadings, the crack path bends, as shown in Figure 8. This is because the asymptotic expressions of the displacement field imposed on the boundary prescribes the target mode-mixity factor only for the initial crack. Our view is that, during the propagation of the crack, the current mode mixity factor on the new crack tip will vary and comparisons with the crack direction criterion written for the initial crack are not any more meaningful. The tangent direction immediately after crack initiation is in agreement with the GMERR criterion also in the simulations of Hakim and Karma (2009), see Figure 6 in Hakim and Karma (2009).

4.3. Strong anisotropy: effect of the mode-mixity factor $K_{\mathrm{II}}/K_{\mathrm{I}}$

We consider the strongly anisotropic fracture surface energy with cubic symmetry in the form $G_c(\theta) = \sqrt[4]{1 + 0.8\cos 4\theta}$, obtained by setting parameters $C_{11} = 1.8$, $C_{12} = -1.7$ and $C_{22} = 0.15$ in (22). The length scale parameter ℓ is set to 0.024, for which the minimal and maximal half-width of the localization band in the phase-field approximation of the crack are $D_{\min} = 2\sqrt[4]{0.2}\ell$ and $D_{\max} = 2\sqrt[4]{1.8}\ell$. The adopted mesh size is $\ell/6$.

Figure 9 reports the results obtained for a pure mode-I loading. To break the symmetry, we introduced a small imperfection by rotating the principal material direction by an angle $\theta_0 = \pi/90$ with respect to the initial crack direction so that the resulting surface energy is $G_c(\theta) = \sqrt[4]{1 + 0.8\cos 4(\theta + \theta_0)}$. The reader can find in Appendix B the standard formula for the rotation of the tensor $\boldsymbol{C}$ in Voigt notation. In the case of a perfect system, the optimal direction of propagation found with GMERR criterion are approximately $\pm 42°$. In our simulation, the imperfection given

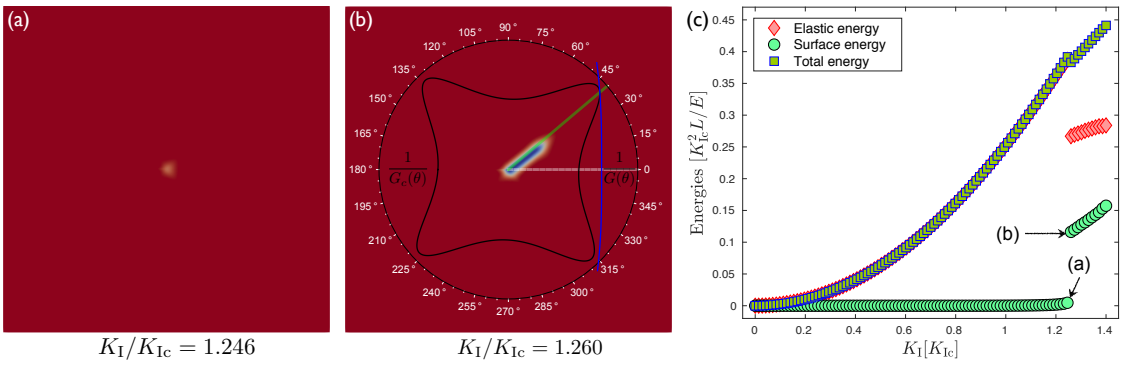

Figure 9: The snapshots of the phase-field simulation with strongly anisotropic fracture surface energy $G_c(\theta) = \sqrt[4]{1 + 0.8\cos 4\,(\theta + \pi/90)}$ under pure Mode-I loading immediately before (a) and after (b) the re-initiation of a crack, and plot of the energies versus the loading parameter K_{I}. Note that the the small diffuse zone ahead of the initial crack tip before the crack re-initiation, and the energetic jump at the re-initiation. In (b) the plot of the phase-field variable is for $K_I = 1.26K_{Ic}$, while the blue line represents the inverse polar plot of the energy release rate $G(\theta)$ for $K_I = K_{Ic}$. K_{Ic} is defined as the critical value of the loading parameter according to the GMERR criterion, corresponding to the tangency condition between the inverse polar plot of $G(\theta)$ and $G_c(\theta)$.

by the small material rotation θ_0 introduces a bias toward the upward direction, as shown by the graphical solution of the GMERR based on the Frank diagrams of the energy release rate $G^{-1}(\theta)$ (in blue) and the fracture surface energy $G_c^{-1}(\theta)$ (in black) in Figure 9(b). When increasing the loading parameter K_{I}, the damage variable α remains 0 away from the initial crack tip until a critical loading at which an add-crack of finite length appears in a single time step, independently of the size of the time-step. The energy diagram of Figure 9(c) clearly shows the discontinuity in time and in space of the evolution, respectively. After that instant, the added crack propagates smoothly. Figure 9(a) and (b) show the damage field α immediately before and immediately after the crack initiation. In the phase-field model the crack initiation happens at $K_I = 1.26K_{Ic}$, where K_{Ic} is the critical load predicted by the GMERR criterion. This overestimate of the critical threshold for the crack initiation is well-known also in isotropic phase-field crack models when the pre-existing crack is modeled as a geometric feature, see Klinsmann et al. (2015) and Tanné et al. (2018). A possible remedy suggested in the isotropic case is to impose the condition $\alpha = 1$ on the pre-existing crack. This is not feasible in the strongly anisotropic surface energy setting, because the pre-existing crack can happen to lie in a forbidden direction. Imposing the condition $\alpha = 1$ on a line aligned to a forbidden direction (Takei et al., 2013; Li et al., 2015) poses numerical, but also mathematical and physical, issues.

Figure 10 shows the results for the kinking angle obtained when varying the mode-mixity factor $K_{\mathrm{II}}/K_{\mathrm{I}}$. In this case we set $\theta_0 = 0$. Figure 10(a) shows the graphical construction of solution of the system of equation (28) and (29) coming from the GMERR criterion. The solution for the optimal propagation angle respecting the tangency condition between the Frank diagram of the surface energy $G_c^{-1}(\theta)$ (in black) and the Frank diagram of the energy release rate $G^{-1}(\theta)$ (in blue) is marked by the green line and the red dot, in the case $K_{\mathrm{II}} < 0$. Varying the mode-mixity factor, the Frank diagram of the energy release rate $G^{-1}(\theta)$ varies in shape, and the intersection point changes accordingly. The blue dots in Figure 10(b) show the optimal crack orientations found in this way as a function of the mode-mixity factor $K_{\mathrm{II}}/K_{\mathrm{I}}$. Red dots are the optimal kinking angle obtained with the phase-field simulations for $K_{\mathrm{II}}/K_{\mathrm{I}} = \{-0.8, -0.01, 0.01, 0.6\}$. As shown also in Figure 10(c), the results of the phase-field simulation are in a very good agreement with the

predictions of the GMERR criterion. The diagram in Figure 10(b) shows a discontinuity of the kinking angle as a function of the mode-mixity factor around $K_{\rm II} = 0$. The kinking angle in pure mode-I is determined by the small perturbations on mode-II, or by other physical or numerical imperfections. This is a peculiar property of the strongly anisotropy surface energy, which is not present in the case of materials with weakly anisotropic surface energy.

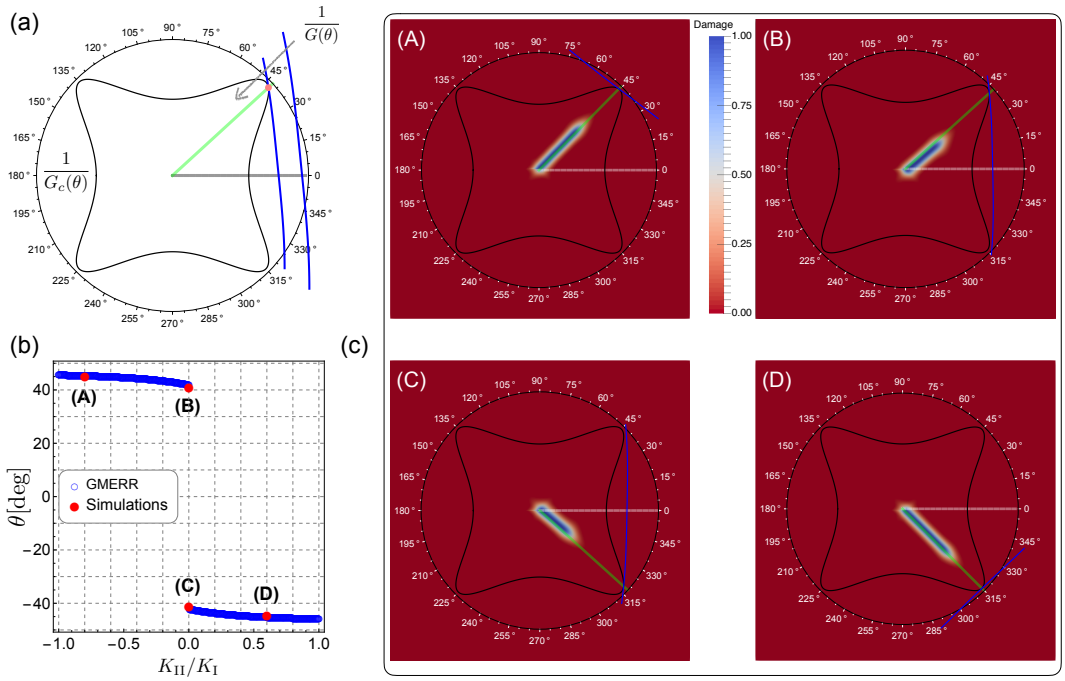

Figure 10: Kinking angle as a function of the mode-mixity factor $K_{\rm II}/K_{\rm I}$ for the strongly anisotropy surface energy $G_c(\theta) = \sqrt[4]{1.0 + 0.8\cos 4\theta}$. (a) Graphical solution of the GMERR criterion; (b) Crack kinking angles as a function of the mode-mixity factor; (c) Snapshots of the damage field α immediately after the kinking for $K_{\rm II}/K_{\rm I} = \{-0.8, -0.01, 0.01, 0.6\}$ (from A to D), superposed with the corresponding graphical solutions of the GMERR criterion.

4.4. Strong anisotropy: effect of the material orientation

We investigate here the effect of material orientation on the kinking direction under pure mode-I loading. We denote by θ_0 the angle determining the orientation of the material frame with respect to the direction of the initial crack, see Figure 11(a). We consider strongly anisotropic fracture surface energy in the form $G_c(\theta) = \sqrt[4]{1 + 0.8\cos 4\,(\theta + \theta_0)}$, as before. We set $C_{11} = 1.8$, $C_{12} = -1.7$ and $C_{22} = 0.15$ in (17) for $\theta_0 = 0°$ and then apply the rotation of the $\mathbf{C}$ tensor as detailed in Appendix B.

Figure 11(b) reports the crack kinking angle θ as function of the material orientation θ_0 found using the GMERR criterion and the phase-field model. Figure 11(c) reports the snapshots of the phase-field variable immediately after the kinking for different material orientations θ_0, together with the graphical construction of the GMERR criterion, from which we extracted the numerical values of the plot in Figure 11(b). The results of the phase-field simulations (in red) are again in excellent agreement with the predictions of the GMERR criterion (in blue). The dependence of the kinking angle on θ_0 is (surprising) almost linear. The behaviour for $\theta_0 < 0$, not reported here, is obviously symmetric, giving, as emphasized in Section 4.3, a jump in the kinking angle around

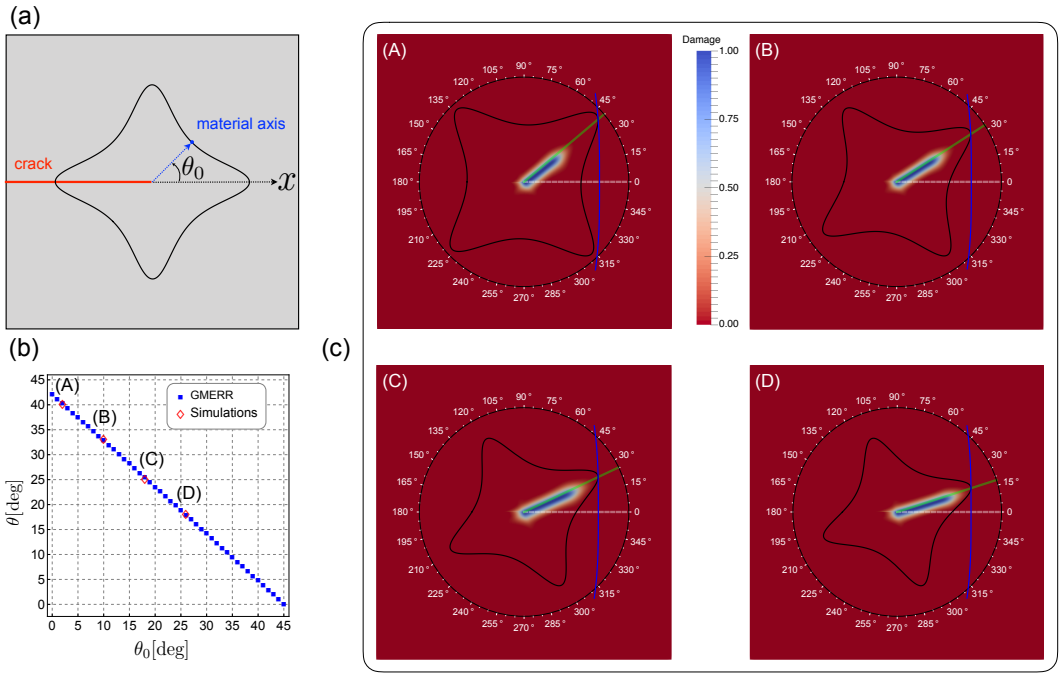

Figure 11: (a) The geometry for the phase-field simulations and polar plot of the $G_c^{-1}(\theta)$, the blue arrow indicates a fixed material direction (one of the strongest directions), and θ_0 denotes the angle between the fixed material direction and the x-axis. (b) The comparison of the crack kinking angle predicted by GMERR criterion with phase-field simulations, the strongly anisotropic surface energy $G_c(\theta) = \sqrt[4]{1 + 0.8\cos(4(\theta + \theta_0))}$ is chosen. (c) The selected phase-field simulations of which the GMERR based graphical constructions place on the top, and the the centre of the graphical construction coincides with the initial crack tip. The crack directions from GMERR predictions are indicated by the green lines, in (A) $\theta_0 = 2°$ and GMERR predicts $\theta = 40°$, in (B) $\theta_0 = 10°$ and GMERR predicts $\theta = 33°$, in (C) $\theta_0 = 18°$ and GMERR predicts $\theta = 25°$ and in (D) $\theta_0 = 26°$ and GMERR predicts $\theta = 18°$.

$\theta_0 = 0$. When the fixed material direction coincides with the x-axis, *i.e.* $\theta_0 = 0°$, the crack kinking directions is determined by small imperfections breaking the symmetry. When one of the weakest material direction coincides with the x-axis, *i.e.* $\theta_0 = 45°$, the crack propagates along the x-axis because of the symmetry of the loading and fracture surface energy.

5. Zig-zag crack patterns in quenched plate with strongly anisotropic surface energy

In this section, we revisit the spectacular quenching experiment of Yuse and Sano (1993) in the case of a brittle material with strongly anisotropic surface energy. The set-up consists in quenching in a cold bath at a constant speed v a pre-cracked hot slab of width $2b$, see Figure 12(a). The temperature of the cold bath is $T_b = T_o - \Delta T$, where T_o is the initial temperature of the slab. In the isotropic case the behavior of system is mainly governed by two dimensionless parameters (Yuse and Sano, 1993; Yang and Ravi-Chandar, 2001; Corson et al., 2009): the thermal diffusion length (Peclet number) $P = bv/D$ and the dimensionless fracture toughness $K_{\rm Ic} = \sqrt{G_0}/E\alpha_T\Delta T\sqrt{b}$, where D is the thermal diffusivity of the strip and α_T is the coefficient of thermal expansion. Provided the velocity of the strip v is not too slow, one can neglect the influence of the crack on the temperature field and approximate the solution of the thermal problem by $T(x) = T_b + (1 - \exp(-P(x - l)))\, H(x - l)$ (Yuse and Sano, 1997), where $H(x)$ is the Heaviside function and

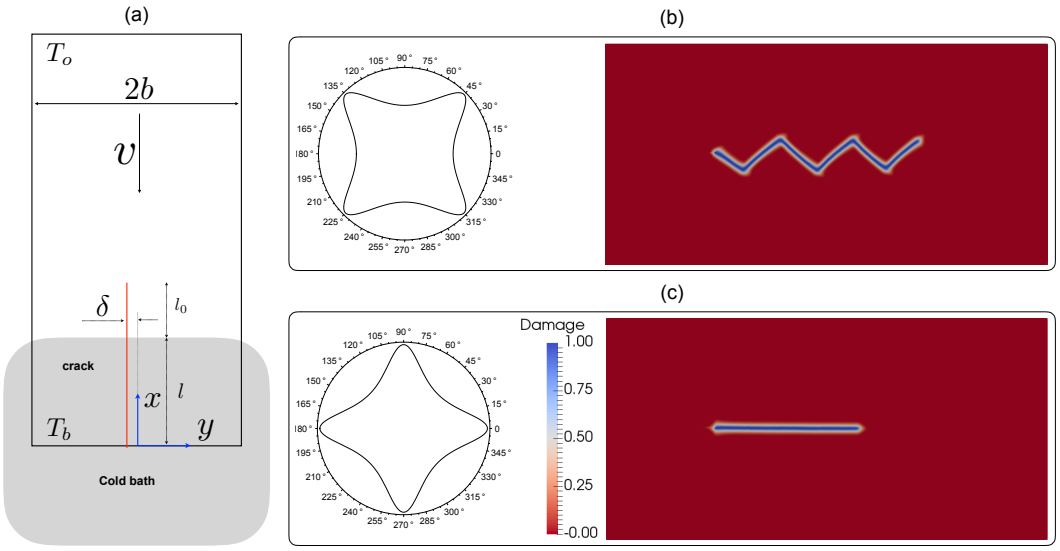

Figure 12: Quenching experiment of a hot slab in a clod bath at a constant speed v. (a) The schematic of the set-up. (b) Result of the numerical simulation of the phase-field model for $G_c(\theta) = G_0 \sqrt[4]{1.0 + 0.8 \cos 4\theta}$ and for parameters $(P, K_{\mathrm{Ic}}) = (12.5, \sqrt{G_0})$ with $G_0 = 0.04$, giving a straight crack in the isotropic surface energy case. (c) Result of the numerical simulation of the phase-field model for $G_c(\theta) = G_0 \sqrt[4]{1.0 - 0.8 \cos 4\theta}$ and for parameters $(P, K_{\mathrm{Ic}}) = (9.6, \sqrt{G_0})$ with $G_0 = 0.0156$, giving an oscillatory crack in the isotropic surface energy case.

$x = l$ corresponds to the surface of the cold bath, as sketched in Figure 12(a). In the case of slab made of isotropic materials, the experiments of Yuse and Sano (1997) and Yang and Ravi-Chandar (2001) showed several possible regimes as a function of the values of P and K_{Ic}, which include the propagation of straight cracks, oscillating cracks, or more complex crack patterns. Adda-Bedia and Pomeau (1995) explained the transition from straight to oscillating cracks through a stability analysis. Subsequently, Corson et al. (2009) were able to reproduce many of these results in numerical simulations based on a phase-field model.

The goal of our simulations is two-fold: (i) to show that the anisotropy of the surface energy can dramatically change the behavior of the system and (ii) to exploit the quenching experiment to closely investigate the properties of crack paths including kinking events. Normalizing the lengths with respect to the width b of the slab, we consider a slab geometry including an initial crack of length $l + l_0$, with an initial immersion length equal to l, see Figure 12(a). Our simulations are for an elastically isotropic material with Poisson's ratio $\nu = 0.23$, an internal length length $\ell = 0.036b$, and a mesh size $h = \ell/6$.

The first simulation is for a fracture toughness where $G_c(\theta) = G_0 \sqrt[4]{1.0 + 0.8 \cos 4\theta}$, for which the quenching direction $\theta = 0$ corresponds to a direction of maximal fracture surface energy, as shown by the Frank-diagram in Figure 12(b). We set the parameters $(P, K_{\mathrm{Ic}}) = (12.5, \sqrt{G_0}) = (12.5, 0.2)$, for which, in the isotropic surface energy setting, the numerical simulations of Corson et al. (2009) and the theoretical analysis of Adda-Bedia and Pomeau (1995) predict the propagation of a straight crack. The results of our phase-field simulations with strongly anisotropic surface energy are reported in Figure 12(b) and show the propagation of crack along a zig-zag path.

In the second simulation, we set $G_c(\theta) = G_0 \sqrt[4]{1.0 - 0.8 \cos 4\theta}$, for which the quenching direction $\theta = 0$ corresponds to a direction of minimal fracture surface energy, and $(P, K_{\mathrm{Ic}}) = (9.6, \sqrt{G_0}) = (9.6, 0.14)$, for which the crack path is oscillatory in the isotropic surface energy case (Adda-Bedia

and Pomeau, 1995; Corson et al., 2009). Our corresponding the phase-field simulation, reported in Figure 12(c), show the propagation of a straight crack.

The two simulations emphasize that in the strongly anisotropic case it is possible to destabilize or stabilize the straight path with a suitable choice of the material orientation. For strongly anisotropic surface energy, the two parameters (P, K_{Ic}) are not any more sufficient to predict the behavior of the system. Therefore, we believe that this problem deserves further numerical and experimental analysis, which is out of the scope of the present work. We refer the interested reader also to Deegan et al. (2003) for preliminary experimental results on the quenching of anisotropic slabs. Interestingly, for many aspects this problem has many analogies to that of the formation of lamellar eutectics in directional solidification (Ghosh et al., 2015).

The zig-zag crack patterns in brittle solids with strongly anisotropic surface energies have been previously reported in experiments (Takei et al., 2013) and phase-field simulations (Li et al., 2015) by imposing reinforcements or unbreakable boundaries to force the crack kinking. It is noteworthy that the zig-zag crack of Figure 12(b) is generated without any artificial boundary conditions. This makes the present set-up particularly well-suited to study the properties of the evolution of crack paths including kinking. Figure 13 focuses on this aspect, reporting, for the case of Figure 12(b), details on the evolution of the crack in time and space. The diagrams in Figure 13(a) of the surface and elastic energy as a function of the time (immersed depth) present jumps corresponding to the kinking events. These jumps are the signature of an unstable (or brutal) propagation of the crack at each kink. Figure 13(b) reports the crack pattern immediately before and immediately after the kink. It shows that the add-crack during the kink is of finite length, independently of the time step. These results are in agreement with the theoretical analysis of Chambolle et al. (2009), which states that kinks must be associated with jumps in time and space of the crack propagation. Chambolle et al. (2009) showed that this property of kinking events holds true also in the isotropic case.

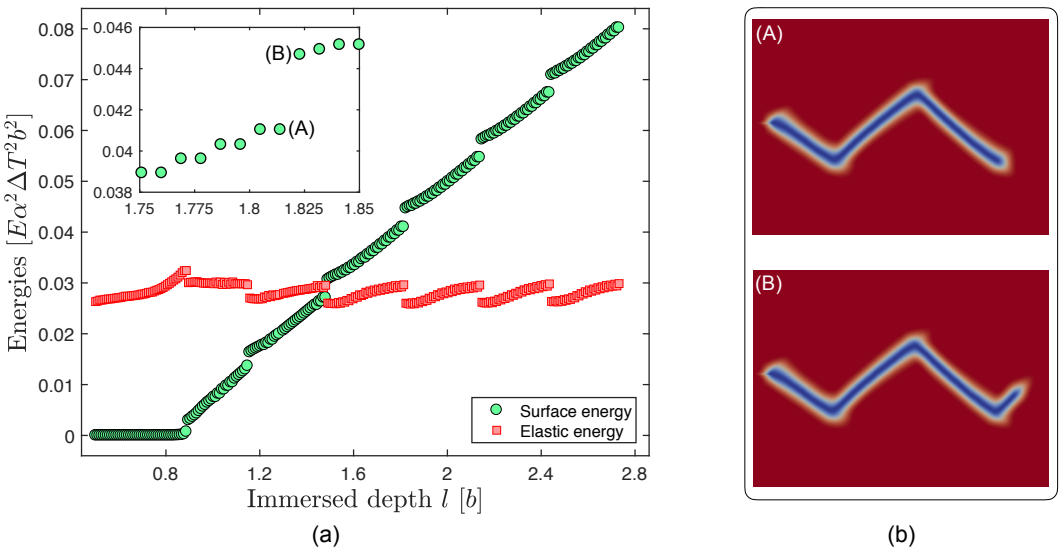

Figure 13: Evolution in time and space of a zig-zag crack pattern during the quenching experiment corresponding to the Figure 12(b). (a) The time-evolution of the surface and elastic energies, including a surface energy jump at each kinking event, as highlighted in the inset. (b) Snapshots of the damage field immediately before (A) and immediately after (B) the crack kinking, showing a finite length add-crack at kinking.

6. Concluding remarks

Anisotropic materials may be classified into two main classes when considering their fracture properties: weakly anisotropic materials where the orientation-dependent fracture surface energy is a convex function of the normal to the crack surface, and strongly anisotropic materials where the fracture toughness is a non-convex function of the normal. The Griffith sharp-interface model becomes ill-posed for strongly anisotropic materials, requiring the use either of a relaxed or a regularized model. In this paper, we developed a variational phase-field model which is intrinsically regularized and can simulate both weakly and strongly anisotropic surface energy. The model is based on the introduction of the second gradient of the phase-field in the energy functional. We developed a dedicated finite-element solver for the associated energy minimization problem. We leverage this numerical tool to revisit the crack kinking problem in the anisotropic setting. The numerical simulations show that the underlying crack path selection criterion of the variational phase-field model is the generalized maximum energy release rate. We studied also the problem of oscillating crack paths in a quenched plate in the case of strongly anisotropic surface energy. Our simulations illustrate how the anisotropy of surface energy can remarkably change the crack patterns, either destabilizing or stabilizing the straight crack path depending on the material orientation. This test case has been selected to give an example of a controlled steady-state crack propagation including kinking events. Echoing with the theoretical analysis of Chambolle et al. (2009), we observed that crack kinking is associated with jumps in time and in space of the crack evolution.

Several aspects of the developed phase-field model are certainly worthy of further refinements. We worked under two key assumptions: (i) including anisotropy only in the surface energy, keeping the elastic energy in its isotropic form; (ii) neglecting the possible crack lip interpenetration issue in compressive crack, without accounting for the asymmetric behavior of cracks in traction and in compression. We believe that the present work constitutes a first necessary step to start tackling this further important issues. Another set of interesting future endeavors can include modeling surface energies characterized by cusp singularities in the Frank diagram representation, as one expects in brittle crystals with cleavage planes, and hexagonal symmetry of the surface energy in the hexagonal crystal system. Moreover, the present work clearly calls for a rigorous mathematical analysis of the properties of regularized models for strongly anisotropic brittle materials.

Appendix A. Crack tip displacement fields and SIFs just after kink

For the convenience of the reader, we recall the expressions of the asymptotic displacement fields around the straight crack tip that have been imposed as the displacement boundary conditions to approximate the singular stress fields around the straight crack tip in our numerical simulations, and of the SIFs $\tilde{K}_{\mathrm{I}}$ and $\tilde{K}_{\mathrm{II}}$ at the tip of a putative crack kinking out the plane of the parent crack at an angle φ and with a vanishing extension of length.

In linear elastic bulk materials, the asymptotic displacement fields around a straight crack tip under mixed Mode I and Mode II load are written as (Zehnder, 2012)

$$\begin{aligned} u_x &= \frac{K_{\mathrm{I}}}{2\mu}\sqrt{\frac{r}{2\pi}}\cos\frac{\varphi}{2}(\kappa-\cos\varphi)+\frac{K_{\mathrm{II}}}{2\mu}\sqrt{\frac{r}{2\pi}}\sin\frac{\varphi}{2}(2+\kappa+\cos\varphi),\\ u_y &= \frac{K_{\mathrm{I}}}{2\mu}\sqrt{\frac{r}{2\pi}}\sin\frac{\varphi}{2}(\kappa-\cos\varphi)+\frac{K_{\mathrm{II}}}{2\mu}\sqrt{\frac{r}{2\pi}}\cos\frac{\varphi}{2}(2-\kappa-\cos\varphi). \end{aligned} \tag{A.1}$$

where $\mu = E/2(1+\nu)$, $\kappa = 3-4\nu$ for plane strain and $\kappa = (3-\nu)/(1+\nu)$ for plane stress, and (r, φ) are polar coordinates with origin positioned at the crack tip.

The SIFs $\tilde{K}_{\mathrm{I}}$ and $\tilde{K}_{\mathrm{II}}$ at the tip of a putative crack kinking out the plane of the parent crack at an angle θ and with a vanishing extension of length, can be expressed as a linear combinations of the SIFs K_{I} and K_{II} at the parent crack tip

$$\tilde{K}_{\mathrm{I}} = F_{11}K_{\mathrm{I}} + F_{12}K_{\mathrm{II}}, \quad \tilde{K}_{\mathrm{II}} = F_{21}K_{\mathrm{I}} + F_{22}K_{\mathrm{II}}. \tag{A.2}$$

The coefficients $F_{ij}\,(i,j=1,2)$ are universal functions which only depends on the kink angle θ and approximately written as power series of $\theta = m\pi\,(-1 < m < +1)$ expanded up to 20th order (Amestoy and Leblond, 1992). These series provide a very accurate approximation of the coefficients F_{ij} for $|\theta| \leq 80°$.

$$\begin{aligned}
F_{11} &= 1 - \frac{3\pi^2}{8}m^2 + \left(\pi^2 - \frac{5\pi^4}{128}\right)m^4 + \left(\frac{\pi^2}{9} - \frac{11\pi^4}{72} + \frac{119\pi^6}{15360}\right)m^6 + 5.0779m^8 \\
&\quad - 2.88312m^{10} - 0.0925m^{12} + 2.996m^{14} - 4.059m^{16} + 1.63m^{18} + 4.1m^{20}, \\
F_{12} &= -\frac{3\pi}{2}m + \left(\frac{10\pi}{3} + \frac{\pi^3}{16}\right)m^3 - \left(2\pi + \frac{133\pi^3}{180} - \frac{59\pi^5}{1280}\right)m^5 + 12.313906m^7 \\
&\quad - 7.32433m^9 + 1.5793m^{11} + 4.0216m^{13} - 6.915m^{15} + 4.21m^{17} + 4.56m^{19}, \\
F_{21} &= \frac{\pi}{2}m - \left(\frac{4\pi}{3} + \frac{\pi^3}{48}\right)m^3 - \left(\frac{2\pi}{3} - \frac{13\pi^3}{30} + \frac{59\pi^5}{3840}\right)m^5 - 6.176023m^7 + 4.44112m^9 \\
&\quad - 1.534m^{11} - 2.07m^{13} + 4.684m^{15} - 3.95m^{17} - 1.32m^{19}, \\
F_{22} &= 1 - \left(4 + \frac{3\pi^2}{8}\right)m^2 + \left(\frac{8}{3} + \frac{29\pi^2}{18} - \frac{5\pi^4}{128}\right)m^4 - \left(\frac{32}{15} + \frac{4\pi^2}{9} + \frac{1159\pi^4}{7200} - \frac{119\pi^6}{15360}\right)m^6 \\
&\quad + 10.58254m^8 - 4.78511m^{10} - 1.8804m^{12} + 7.28m^{14} - 7.591m^{16} + 0.25m^{18} + 12.5m^{20}.
\end{aligned} \tag{A.3}$$

Appendix B. Rotation of material orientation relative to the sample

Here we summarize how to transform second order tensor $\mathbf{B}$ and fourth order tensor $\mathbf{C}$ to a coordinate system that does not coincide with the principal material axes. The basis change formula for second order tensors are like strain and stress, very easy to derive. Suppose that the components of the second order tensor are given in basis $\boldsymbol{e}$, and we want to determine its components in a second basis $\boldsymbol{e}'$. The change of basis formula for the second order tensor $\mathbf{B}$ is written as

$$\mathbf{B}' = \mathbf{Q}\mathbf{B}\mathbf{Q}^{\mathrm{T}}, \tag{B.1}$$

where $\mathbf{Q}$ is a transformation matrix (Holzapfel, 2000). In two-dimensional setting, when we rotate the material about the third coordinate vector by an angle Θ, the transformation matrix reduces to the Mohr transformation

$$\mathbf{Q} = \begin{pmatrix} \cos\Theta & -\sin\Theta \\ \sin\Theta & \cos\Theta \end{pmatrix}.$$

In contrast, the basis change formula for fourth order tensors in Voigt notation are not straightforward. The change of basis formula for the fourth order tensor expressed as a matrix in Voigt

notation $\mathbf{C}$ can be expressed in matrix form as

$$\mathbf{C}' = \mathbf{K}\mathbf{C}\mathbf{K}^{\mathrm{T}}, \tag{B.2}$$

where $\mathbf{K}$ is a transformation matrix (Ting, 1996). In three-dimensional setting, when we rotate the material about the third coordinate vector by an angle Θ, the transformation matrix reduces to

$$\mathbf{K} = \begin{pmatrix} c^2 & s^2 & 0 & 0 & 0 & 2cs \\ s^2 & c^2 & 0 & 0 & 0 & -2cs \\ 0 & 0 & 1 & 0 & 0 & 0 \\ 0 & 0 & 0 & c & -s & 0 \\ 0 & 0 & 0 & s & c & 0 \\ -cs & cs & 0 & 0 & 0 & c^2 - s^2 \end{pmatrix},$$

where $c = \cos\Theta, s = \sin\Theta$. Consequently, in two dimension, the transformation matrix for the 3×3 Voigt representation of the fourth-order tensor (18) is just

$$\mathbf{K} = \begin{pmatrix} c^2 & s^2 & 2cs \\ s^2 & c^2 & -2cs \\ -cs & cs & c^2 - s^2 \end{pmatrix}.$$

Acknowledgement

This work was partially supported by the `FRZX026-SU-16-R-EMR-02-ANIS` Sorbonne University *Emergence* project, which is gratefully acknowledged. BL was supported by a Labex *CalsimLab* fellowship/scholarship. The Labex CalsimLab, reference `ANR-11-LABX-0037-01`, is funded by the program "Investissements d'avenir" of the French *Agence Nationale de la Recherche*, reference `ANR-11-IDEX-0004-02`. This work was granted access to the HPC resources of the HPCaVe center at Sorbonne Université.

The authors thank Jean-Francois Babadjian (Paris-Orsay) and Flaviana Iurlano (Sorbonne University) for helpful discussions on the subject of this work.

References

Abinandanan, T., Haider, F., 2001. An extended cahn-hilliard model for interfaces with cubic anisotropy. Philosophical Magazine A 81, 2457–2479.

Adda-Bedia, M., Pomeau, Y., 1995. Crack instabilities of a heated glass strip. Physical Review E 52, 4105.

Alnæs, M., Blechta, J., Hake, J., Johansson, A., Kehlet, B., Logg, A., Richardson, C., Ring, J., Rognes, M.E., Wells, G.N., 2015. The fenics project version 1.5. Archive of Numerical Software 3, 9–23.

Ambrosio, L., 1990. Existence theory for a new class of variational problems. Archive for Rational Mechanics and Analysis 111, 291–322.

Ambrosio, L., Fusco, N., Pallara, D., 2000. Functions of bounded variation and free discontinuity problems. Oxford University Press.

Ambrosio, L., Tortorelli, V.M., 1990. Approximation of functional depending on jumps by elliptic functional via Gamma-convergence. Communications on Pure and Applied Mathematics 43, 999–1036.

Amestoy, M., Leblond, J., 1992. Crack paths in plane situations–II. detailed form of the expansion of the stress intensity factors. International Journal of Solids and Structures 29, 465–501.

Amor, H., Marigo, J.J., Maurini, C., 2009. Regularized formulation of the variational brittle fracture with unilateral contact: numerical experiments. Journal of the Mechanics and Physics of Solids 57, 1209–1229.

Azhdari, A., Nemat-Nasser, S., Rome, J., 1998. Experimental observations and computational modeling of fracturing in an anisotropic brittle crystal (sapphire). International Journal of Fracture 94, 251–266.

Balay, S., Abhyankar, S., Adams, M.F., Brown, J., Brune, P., Buschelman, K., Dalcin, L., Eijkhout, V., Gropp, W.D., Kaushik, D., Knepley, M.G., McInnes, L.C., Rupp, K., Smith, B.F., Zampini, S., Zhang, H., Zhang, H., 2016. PETSc Users Manual. Technical Report ANL-95/11 - Revision 3.7. Argonne National Laboratory.

Ball, A., Payne, B., 1976. The tensile fracture of quartz crystals. Journal of Materials Science 11, 731–740.

Bleyer, J., Alessi, R., 2018. Phase-field modeling of anisotropic brittle fracture including several damage mechanisms. Computer Methods in Applied Mechanics and Engineering 336, 213–236.

Borden, M.J., Hughes, T.J., Landis, C.M., Verhoosel, C.V., 2014. A higher-order phase-field model for brittle fracture: Formulation and analysis within the isogeometric analysis framework. Computer Methods in Applied Mechanics and Engineering 273, 100–118.

de Borst, R., Chen, L., 2018. The role of bézier extraction in adaptive isogeometric analysis: Local refinement and hierarchical refinement. International journal for numerical methods in engineering 113, 999–1019.

Bourdin, B., 2007. Numerical implementation of the variational formulation for quasi-static brittle fracture. Interfaces and Free Boundaries 9, 411–430.

Bourdin, B., Francfort, G., Marigo, J.J., 2000. Numerical experiments in revisited brittle fracture. Journal of the Mechanics and Physics of Solids 48, 797–826.

Bourdin, B., Francfort, G., Marigo, J.J., 2008. The variational approach to fracture. Journal of Elasticity 91, 5–148.

Burger, M., Esposito, T., Zeppieri, C.I., 2015. Second-order edge-penalization in the ambrosio–tortorelli functional. Multiscale Modeling & Simulation 13, 1354–1389.

Chambolle, A., Francfort, G., Marigo, J.J., 2009. When and how do cracks propagate? Journal of the Mechanics and Physics of Solids 57, 1614–1622.

Chandler, M., Meredith, P., Brantut, N., Crawford, B., 2016. Fracture toughness anisotropy in shale. Journal of Geophysical Research: Solid Earth 121, 1706–1729.

Chapelle, D., Bathe, K.J., 2010. The Finite Element Analysis of Shells - Fundamentals. Second edition. ed., Springer Science & Business Media.

Clayton, J., Knap, J., 2014. A geometrically nonlinear phase field theory of brittle fracture. International Journal of Fracture 189, 139–148.

Corson, F., Adda-Bedia, M., Henry, H., Katzav, E., 2009. Thermal fracture as a framework for quasi-static crack propagation. International journal of fracture 158, 1–14.

Cotterell, B., Rice, J., 1980. Slightly curved or kinked cracks. International Journal of Fracture 16, 155–169.

Deegan, R.D., Chheda, S., Patel, L., Marder, M., Swinney, H.L., Kim, J., de Lozanne, A., 2003. Wavy and rough cracks in silicon. Physical Review E 67, 066209.

Di Carlo, A., Gurtin, M.E., Podio-Guidugli, P., 1992. A regularized equation for anisotropic motion-by-curvature. SIAM Journal on Applied Mathematics 52, 1111–1119.

Durán, R., Liberman, E., 1992. On mixed finite element methods for the reissner-mindlin plate model. Mathematics of Computation 58, 561–573.

Ebrahimi, F., Hussain, S., 1995. Crack path in single crystals. Scripta Metallurgica et Materialia 32, 1507–1511.

Ebrahimi, F., Kalwani, L., 1999. Fracture anisotropy in silicon single crystal. Materials Science and Engineering: A 268, 116–126.

Eggleston, J., McFadden, G., Voorhees, P., 2001. A phase-field model for highly anisotropic interfacial energy. Physica D: Nonlinear Phenomena 150, 91–103.

Erdogan, F., Sih, G., 1963. On the crack extension in plates under plane loading and transverse shear. Journal of Basic Engineering 85, 519–527.

Farrell, P., Maurini, C., 2017. Linear and nonlinear solvers for variational phase-field models of brittle fracture. International Journal for Numerical Methods in Engineering 109, 648–667.

Focardi, M., 2001. On the variational approximation of free-discontinuity problems in the vectorial case. Mathematical Models and Methods in Applied Sciences 11, 663–684.

Fonseca, I., 1992. Lower semicontinuity of surface energies. Proceedings of the Royal Society of Edinburgh Section A: Mathematics 120, 99–115.

Francfort, G., Marigo, J.J., 1998. Revisiting brittle fracture as an energy minimization problem. Journal of the Mechanics and Physics of Solids 46, 1319–1342.

Ghosh, S., Choudhury, A., Plapp, M., Bottin-Rousseau, S., Faivre, G., Akamatsu, S., 2015. Interphase anisotropy effects on lamellar eutectics: A numerical study. Physical Review E 91, 022407.

Gol'Dstein, R., Salganik, R., 1974. Brittle fracture of solids with arbitrary cracks. International Journal of Fracture 10, 507–523.

Griffith, A., 1921. The phenomena of rupture and flow in solids. Philosophical Transactions of the Royal Society of London A: Mathematical, Physical and Engineering Sciences 221, 163–198.

Gurtin, M., 2008. Configurational forces as basic concepts of continuum physics. volume 137. Springer Science & Business Media.

Gurtin, M., Podio-Guidugli, P., 1998. Configurational forces and a constitutive theory for crack propagation that allows for kinking and curving. Journal of the Mechanics and Physics of Solids 46, 1343–1378.

Gurtin, M.E., 1993. Thermomechanics of evolving phase boundaries in the plane. Oxford University Press.

Gurtin, M.E., Jabbour, M.E., 2002. Interface evolution in three dimensions with curvature-dependent energy and surface diffusion: Interface-controlled evolution, phase transitions, epitaxial growth of elastic films. Archive for Rational Mechanics and Analysis 163, 171–208.

Hakim, V., Karma, A., 2005. Crack path prediction in anisotropic brittle materials. Physical Review Letters 95, 235501.

Hakim, V., Karma, A., 2009. Laws of crack motion and phase-field models of fracture. Journal of the Mechanics and Physics of Solids 57, 342–368.

Hale, J.S., Brunetti, M., Bordas, S.P., Maurini, C., 2018. Simple and extensible plate and shell finite element models through automatic code generation tools. Computers & Structures 209, 163–181.

Hamm, E., Reis, P., LeBlanc, M., Roman, B., Cerda, E., 2008. Tearing as a test for mechanical characterization of thin adhesive films. Nature materials 7, 386–390.

Herring, C., 1951. Some theorems on the free energies of crystal surfaces. Physical Review 82, 87.

Holzapfel, G.A., 2000. Nonlinear Solid Mechanics: A Continuum Approach for Engineering. John Wiley & Sons Ltd.

Hussain, M., Pu, S., Underwood, J., 1974. Strain energy release rate for a crack under combined mode I and mode II, in: Fracture Analysis: Proceedings of the 1973 National Symposium on Fracture Mechanics, Part II, ASTM International. pp. 2–28.

Ibarra, A., Roman, B., Melo, F., 2016. The tearing path in a thin anisotropic sheet from two pulling points: Wulff's view. Soft Matter 12, 5979–5985.

Ichikawa, M., Tanaka, S., 1982. A critical analysis of the relationship between the energy release rate and the stress intensity factors for non-coplanar crack extension under combined mode loading. International journal of Fracture 18, 19–28.

Judt, P., Ricoeur, A., Linek, G., 2015. Crack path prediction in rolled aluminum plates with fracture toughness orthotropy and experimental validation. Engineering Fracture Mechanics 138, 33–48.

Judt, P.O., Zarges, J.C., Ricoeur, A., Heim, H.P., 2018. Anisotropic fracture properties and crack path prediction in glass and cellulose fiber reinforced composites. Engineering Fracture Mechanics 188, 344–360.

Khan, A., Vincent, J., 1993. Anisotropy in the fracture properties of apple flesh as investigated by crack-opening tests. Journal of Materials Science 28, 45–51.

Klinsmann, M., Rosato, D., Kamlah, M., McMeeking, R.M., 2015. An assessment of the phase field formulation for crack growth. Computer Methods in Applied Mechanics and Engineering 294, 313–330.

Kobayashi, R., Giga, Y., 2001. On anisotropy and curvature effects for growing crystals. Japan Journal of Industrial and Applied Mathematics 18, 207–230.

Li, B., Millán, D., Torres-Sáncheza, A., Roman, B., Arroyo, M., 2018. A variational model of fracture for tearing brittle thin sheets. Journal of the Mechanics and Physics of Solids 119, 334–348.

Li, B., Peco, C., Millán, D., Arias, I., Arroyo, M., 2015. Phase-field modeling and simulation of fracture in brittle materials with strongly anisotropic surface energy. International Journal for Numerical Methods in Engineering 102, 711–727.

Marder, M., 2004. Cracks cleave crystals. EPL (Europhysics Letters) 66, 364.

Marigo, J.J., Maurini, C., Pham, K., 2016. An overview of the modelling of fracture by gradient damage models. Meccanica 51, 3107–3128.

Mitchell, N.P., Koning, V., Vitelli, V., Irvine, W.T., 2017. Fracture in sheets draped on curved surfaces. Nature Materials 16, 89–93.

Mouhat, F., Coudert, F.X., 2014. Necessary and sufficient elastic stability conditions in various crystal systems. Physical Review B 90, 224104.

Müller, P., Métois, J., 2008. Anisotropy of the surface thermodynamic properties of silicon. Thin Solid Films 517, 65–68.

Mumford, D., Shah, J., 1989. Optimal approximations by piecewise smooth functions and associated variational problems. Communications on Pure and Applied Mathematics 42, 577–685.

Nam, K.H., Park, I.H., Ko, S.H., 2012. Patterning by controlled cracking. Nature 485, 221–224.

Nasseri, M., Mohanty, B., 2008. Fracture toughness anisotropy in granitic rocks. International Journal of Rock Mechanics and Mining Sciences 45, 167–193.

Nguyen, T.T., Réthoré, J., Baietto, M.C., 2017. Phase field modelling of anisotropic crack propagation. European

Journal of Mechanics-A/Solids 65, 279–288.
Palaniswamy, K., Knauss, W., 1978. On the problem of crack extension in brittle solids under general loading, in: Nemat-Nasser, S. (Ed.), Mechanics Today. Pergamon Press. volume 4, pp. 87–184.
Pham, K., Amor, H., Marigo, J.J., Maurini, C., 2011. Gradient damage models and their use to approximate brittle fracture. International Journal of Damage Mechanics 20, 618–652.
Rockafellar, R.T., 1997. Convex Analysis. Princeton University Press.
Roman, B., 2013. Fracture path in brittle thin sheets: a unifying review on tearing. International Journal of Fracture 182, 209–237.
Romero, V., Roman, B., Hamm, E., Cerda, E., 2013. Spiral tearing of thin films. Soft Matter 9, 8282–8288.
Schultz, R.A., Bradt, R.C., 1992. Cleavage of ceramic and mineral single crystals, in: Fracture Mechanics of Ceramics. Springer, pp. 135–153.
Sekerka, R.F., 2005. Analytical criteria for missing orientations on three-dimensional equilibrium shapes. Journal of Crystal Growth 275, 77–82.
Sumi, Y., 2014. Mathematical and Computational Analyses of Cracking Formation. volume 2. Springer.
Takei, A., Roman, B., Bico, J., Hamm, E., Melo, F., 2013. Forbidden directions for the fracture of thin anisotropic sheets: an analogy with the wulff plot. Physical Review Letters 110, 144301.
Tanné, E., Li, T., Bourdin, B., Marigo, J.J., Maurini, C., 2018. Crack nucleation in variational phase-field models of brittle fracture. Journal of the Mechanics and Physics of Solids 110, 80–99.
Ting, T.C.T., 1996. Anisotropic elasticity: Theory and Applications. Oxford University Press.
Torabi, S., Lowengrub, J., 2012. Simulating interfacial anisotropy in thin-film growth using an extended cahn-hilliard model. Physical Review E 85, 041603.
Torabi, S., Lowengrub, J., Voigt, A., Wise, S., 2009. A new phase-field model for strongly anisotropic systems. Proceedings of the Royal Society of London A: Mathematical, Physical and Engineering Sciences 465, 1337–1359.
Yang, B., Ravi-Chandar, K., 2001. Crack path instabilities in a quenched glass plate. Journal of the Mechanics and Physics of Solids 49, 91–130.
Yuse, A., Sano, M., 1993. Transition between crack patterns in quenched glass plates. Nature 362, 329–331.
Yuse, A., Sano, M., 1997. Instabilities of quasi-static crack patterns in quenched glass plates. Physica D: Nonlinear Phenomena 108, 365–378.
Zehnder, A., 2012. Fracture Mechanics (Lecture Notes in Applied and Computational Mechanics). Springer Netherlands.